Egypt. J. of Appl. Sci., 40 (5-6) 2025 *25-60*

TRACING MAGMATIC PHYSICOCHEMICAL CONDITIONS IN ABU KHARIEF ALKALI GRANITE, NORTH-EASTERN DESERT, EGYPT EVIDENCES FROM APATITE, MAGNETITE & ILMENITE CHEMISTRY

Moustafa M. Mogahed
Geology Department, Faculty of Science, Benha University, Benha, Egypt.
E-mail- mustafa.ahmed01@fsc.bu.edu.eg

ABSTRACT

The Abu Kharif Alkali Granite (AKAG) complex in the Northern Eastern Desert consists of syenogranite and alkali feldspar granite. Although the petrogenesis of these rocks is well-known in geologic literatures. Their physical-chemical condition has not been conducted based on the chemical composition of their mineral constituents. Whole-rock geochemical data classify AKAG as highly fractionated A-type with alkaline affinity and an A1 subtype. The mineral chemistry of feldspars, biotite, apatite, and iron oxides was used to determine the physical and chemical conditions and the development of the alkali granite. Whole-rock geochemical data revealed that these rocks possess $(La/Sm)_n$ = 1.71-4.52, mild HREE depletion $(Gd/Yb)_n$ = 1.34-3.11, and pronounced negative Eu anomalies (Eu/Eu* = 0.09-0.37), characteristic of highly fractionated A-type granites. The biotite thermometer yields crystallization temperature ranges from 610 to 700°C at oxygen fugacity (logfO2) -11.91 and -12.63, which indicates crystallization from relatively oxidized magma that is consistent with low-pressure emplacement. The chemical data for magnetite, ilmenite, and apatite showed that the magmatic oxygen fugacities of the AKAG were a bit higher than the ΔNNO buffer line, and that magnetite and ilmenite were stable at temperatures between 571 and 678°C, which suggests that the oxygen levels decreased as the magma evolved. The rare earth element (REE) patterns of apatite from AKAG show a moderate to strong increase in light REEs (LREEs) like La, Ce, and Pr, along with a small to moderate decrease in Eu (Eu/Eu* < 1), which probably indicates that plagioclase was separated out during the development of the magma. The relatively flat HREE patterns and slight depletion in Y in apatite suggest the absence or minimal involvement of garnet in the residual melt. The trace elements in apatite match the usual characteristics of advanced A-type granites and suggest that apatite formed in conditions with plenty of oxygen. The parental melts of the studied granite were likely F-rich and Cl-poor which supports the high F/Cl ratios derived from apatite compositions. High F/Cl ratios observed in apatite from the studied granitic rocks resulted from a combination of an intrinsically high F/Cl ratio in the melt and the effects of fluid exsolution and

degassing during late-stage magmatic evolution. The analyzed apatite data suggest that AKYG underwent late-stage melt-fluid interaction associated with volatile exsolution during crystallization. Apatite samples display low Ce/Pb (0.06-0.395) and Th/U (1.87-12.37), which strongly reflect the involvement of fluid and crustal material during crystallization and imply that the genesis of the AKAG was through partial melting of crustal sources.

Key Words: Arabian-Nubian Shield; Alkali granite; Apatite, Pressure; Temperature, Oxygen fugacity; crustal source**.**

INTRODUCTION

The Arabian–Nubian Shield (ANS) represents one of the largest and well-preserved Neoproterozoic juvenile continental crustal provinces on the earth, formed during the assembly of Gondwana through the convergence and closure of the Mozambique Ocean **(Stern, 1994 ; Jacobs & Thomas, 2004 and Johnson *et al.*, 2011)**. As the northern extension of the East African Orogen (EAO), the ANS is characterized by a complex collage of arc terranes, ophiolitic assemblages, and syn- to post-collisional plutons that crystallized during a prolonged tectono-magmatic evolution spanning from ~870 to 540 Ma **(Stern, *et al.*, 2004 and Fritz *et al.*, 2013)**. This evolution is typically divided into two magmatic stages: an earlier Cryogenian orogenic phase dominated by calc-alkaline arc-related intrusions and a later Ediacaran post-collisional phase marked by widespread emplacement of felsic granites.

In Egypt, the ANS is subdivided into the Northern, Central, and Southern Eastern Desert terranes **(Stern and Hedge, 1985)**. The Northern Eastern Desert (NED) is particularly enriched in post-orogenic granitoids, Dokhan volcanics, and molasse-type Hammamat sediments **(Eliwa *et al.*, 2014 and Stern *et al.*, 2020)**. Granitoid rocks in the Eastern Desert are broadly categorized into older (Cryogenian; 850–635 Ma) and younger (Ediacaran; 635–541 Ma) suites **(El-Bialy and Omar, 2015 and El-Bahariya, 2019)**. The older granites are mainly tonalitic to granodioritic I-type compositions, often interpreted to form through fractional crystallization of mantle-derived magmas with varying degrees of crustal interaction **(Moghazi, 1999 and Farahat, *et al.*, 2007)**. In contrast, the younger granites exhibit more evolved geochemical signatures, including both highly fractionated I-type and A-type affinities, and are often interpreted to result from partial melting of crustal sources or hybridization between juvenile mantle melts and older crustal material **(Farahat and Azer, 2011 ; Mogahed and Abdelfadil, 2021)**.

The Abu-Kharif granite complex, located north of the Safaga-Qena Tectonic Discontinuity (SQTD) and represents one of the most distinctive Ediacaran granitic massifs in the north Eastern Desert **(Abdel Wanees, *et al.*, 2021 and Dessouky *et al.*, 2024)**. Previous geological mapping and geochronological work identified the complex as consisting of multiple intrusive phases, including granodiorite, monzogranite, and alkali-feldspar

riebeckite granite, interpreted to have formed during Cambrian post-collisional extension (~522 Ma; **Abdel-Rahman, 2006**). Field and petrographic evidence suggest a multi-stage magmatic evolution with local enrichment in tungsten (W) and rare metals, especially in association with the more evolved granitic units **(Helba, *et al.*,1997; Moghazi, Iaccheri, Bakhsh, Kotov, and Ali, 2015)**.

Despite its mineralogical diversity and economic interest, the petrogenesis and tectonomagmatic significance of the Abu-Kharif granites remain poorly constrained. In particular, the processes governing compositional diversity, magma source characteristics, and potential for metal enrichment are not fully understood. Recent advances in accessory mineral geochemistry, particularly apatite, offer a promising avenue for resolving these questions. Apatite incorporates a wide range of trace elements (e.g., REEs, Sr, Mn, U, Th) and halogens (F, Cl), making it a sensitive recorder of melt composition, redox state, temperature, and fluid evolution **(Pan and Fleet, 2002 ; Piccoli and Candela, 2002 and Miles *et al.*, 2014)**. Its resistance to post-magmatic alteration also makes it an ideal proxy for reconstructing magmatic processes in evolved granites where feldspars or biotite may be altered **(Miles *et al.*, 2014)**.

Apatite regarded as an ubiquitous accessory in granitic rocks, that is suggested to be a common indicator for assisting the petrogenetic evolution and to constrain magma sources of granitoid systems **(Chu *et al.*, 2009 and Miles *et al.*, 2014)**. Its crystal structure readily incorporates volatile elements like F, Cl, and OH, along with trace elements such as Sr, Y, U, Th, and various rare-earth elements, making it an ideal recorder of melt chemistry, redox conditions, and magmatic differentiation stages **(Chu *et al.*, 2009).**

The geology, petrographic description, geochemical features as well as the petrogenesis of Abu Kharief alkali granites are well-known as it subjected to comprehensive investigations by numerous geologic literature **(e.g., Abdel Wanees *et al.*, 2021 and Dessouky *et al.*, 2024)**. This study aims to investigate the physicochemical conditions during the magmatic evolution of the Abu Karief alkali granite, magma source, and volatile compositions using the chemical compositions of feldspars, biotite, apatite and magnetite- ilmenite minerals. The results contribute to a broader understanding of crustal evolution and granite petrogenesis in post-collision magmatic systems.

Geological Setting and petrography of the Abukharief Alkali Granite Complex.

The North Eastern Desert (NED), where the Abu-Kharif area is located, is characterized by the dominance of Cryogenian arc-related complexes, ophiolitic mélanges, and high-level granitoids. It is structurally bounded to the north by SQTD, a major NW–SE crustal structure interpreted as a terrane boundary or a reactivated shear zone associated with

late Neoproterozoic deformation **(El-Gaby *et al.*, 1988 ; Stern and Ali, 2020 ; Abd El-Wahed *et al.*, 2022 and Lashin *et al.*, 2023)**. North of this discontinuity, post-collisional felsic plutonism becomes increasingly voluminous, forming large composite batholiths and anorogenic granite complexes that intrude older supracrustal and arc-derived assemblages **(Johnson *et al.*, 2011 and Mansour *et al.*, 2025)**.

The Abu-Kharif granitic complex (AKGC) lies immediately north of the SQTD between latitudes 26° 37′ and 26° 50′ N and longitudes 33° 20′ and 33° 28′ E (Fig. 1). The geologic setting of Abu Kharief area is well-documented through various geologic literature **(e.g., Abdel Wanees *et al.*, 2021 and Dessouky *et al.*, 2024)** and it will be summarized in the next paragraphs.

The area of Abu Kharief comprises several intrusive phases emplaced into older metavolcanic rocks (Fig. 1b). Abu Kharief area constitutes a variety of magmatic lithologies including metavolcanic rocks, granodiorite, monzogranite, and alkali granite (Figs. 1b; 2a-d). Except for the alkali granite, these formations are frequently intersected by basic dikes and quartz veins. The granitic rocks exhibit sharp intrusive contacts between each other as well as with their host metavolcanic rocks (Figs. 2a-e).

The Abu-Kharif area is underlain by a suite of Neoproterozoic to Cambrian igneous and metamorphic rocks, emplaced in a structurally complex zone north of the SQTD (Fig. 1b) **(Asran, *et al.*, 2017)**. Country rocks consist primarily of fine- to medium-grained metavolcanics, ranging in composition from andesitic to rhyolitic (Fig. 2) **(Abdel-Rahman, 2006)**. These units are variably foliated and exhibit mineral assemblages dominated by plagioclase, chlorite, epidote, and quartz, indicative of low-grade greenschist facies metamorphism. The metavolcanic unit is considered to record a Cryogenian subduction-related tectonic event and represents the oldest lithology within the investigated area **(El-Shazly and El-Sayed, 2000)**. These rocks are internally diverse, displaying significant differences in color index, grain size, and mineralogical composition. They comprise both acidic varieties (metadacite and metarhyolite) and metabasalt, the latter exhibiting mild foliation indicative of greenschist-facies metamorphism.

Granodiorite is the predominant rock type within the study area (Fig. 1ba). Previously it was assigned as late-tectonic I-type granites (~650 Ma) (e.g., **Moghazi, 1999 ; El-Shazly and El-Sayed, 2000**). The granodiorite is cut by numerous basic dike swarms, although some felsic dikes are present. Its coarse texture often leads to surface exfoliation and consists of massive to irregularly rounded or sub-rounded mafic xenoliths with sharply defined boundaries (Fig. 2g and i). The granodiorite intruded into metavolcanic rocks, and itself is sharply intruded by the monzogranite and alkali granite (Fig. 2c and d).

Monzogranite occurs at the southern part of AKCG (Fig. 1b), where it intruded into both metavolcanics and granodiorite. The monzogranite forms relatively smooth outcrops with moderate to low elevation and shows significant weathering where exfoliation and jointing are widespread (Fig. 2f). The rock is medium- to coarse-grained, typically ranging in color from whitish-pink to light pink, and displays joint sets trending predominantly N–S and NE–SW. Notably, the monzogranite hosts a series of tungsten-bearing quartz veins, especially concentrated in the southern flank of Mount Abu Kharif (Fig. 1b).

The younger granitic rocks, which is the main objective of this study, represent the less abundant granitic rocks within the Abu-Kharif area, which occur as two major phases: syenogranite and alkali feldspar granite. These rocks are generally unfoliated and intruded into both the older granitoids and country rocks (Figs. 2b and f). They are distinguished in the field by their pink to red coloration, high silica content, and relatively coarse grain size with highly jointed appearance (Fig. 2e) and locally traversed by fluorite veins (Fig. 2j). The alkali granite in the Abu Kharif region has been radiometrically dated to the Cambrian with an age of 522 ± 21 Ma as an anorogenic A-type intrusive pluton **(El-Sayed 1998 and Abdel-Rahman 2006).** This granite forms rugged, mountainous ridges and intrudes sharply into adjacent country rocks (see Fig. 3d). Texturally, it is leucocratic, with medium- to coarse-grained crystals, and varies in color from pink to red.

Petrography

The Abu-Kharif alkali granites is dominated by two felsic intrusive phases—syenogranite and alkali feldspar granite which will discussed only in this study—that vary in texture, mineral assemblage, and degree of magmatic differentiation. These units are unfoliated, exhibit typical plutonic textures, and intruded older country rocks, including metavolcanics, granodiorite and monzogranite. Both granitic phases display a range of accessory minerals, including apatite and Fe-oxides.

Microscopically the two phases have similar mineral assemblage (quartz, alkali feldspars and plagioclase occur as essential minerals). In syenogranite, plagioclase typically appears as large, well-formed (euhedral) crystals exhibiting clear magmatic zoning. In contrast, plagioclase in alkali-feldspar granite occurs as unzoned crystals (Fig. 3a). K-feldspar in both rock types is characterized by perthitic orthoclase—displaying flame-, patch-, and cross-hatched textures—with subordinate microcline (Fig. 3b). Quartz grains are anhedral to subhedral, often showing undulatory extinction (Fig. 3a-c), and locally form complex intergrowths such as granophyric and myrmekitic textures.

In alkali-feldspar granite, quartz displays intriguing relationships with the surrounding K-feldspars (Fig. 3d–f) it is commonly found enclosed by perthite or occupying interstitial spaces between quartz and plagioclase,

without trapping earlier-formed phases. This suggests that quartz and perthite crystallized at nearly identical temperatures, where quartz encloses laths of perthite and albite (Fig. 3d).

These textural and mineralogical features shed light on the crystallization sequence and thermal history of these granites, reflecting synchronized growth of quartz and feldspar during the late magmatic stages. The myrmekitic and granophyric intergrowths further imply complex magmatic-fluid interactions during cooling. In addition, muscovite in syenogranite typically occurs anhedral grains, replacing biotite, whereas in alkali-feldspar granite it predominantly replaces perthite and biotite. These textures strongly suggest a secondary (alteration-related) origin. Nevertheless, fine euhedral muscovite crystals are occasionally found within quartz (Fig. 3e and f), indicating minor primary crystallization.

Apatite occurs in both granitic types, where it mostly occurs as acicular grain, whereas sometimes occur as subhedral grains (Fig. 3d and e). Apatite within syenogranite is always associated with biotite, whereas within alkali feldspar granite it usually occurs within feldspars (Fig. 3h).

Secondary alterations in both granitic types, including sericitization of feldspars, chloritization of biotite, and epidotization of fracture planes, are apparent. Moreover,the mineral assemblage and texture suite the studied SG and AKG to point to crystallization from a volatile-rich, peralkaline, high-temperature A-type melt emplaced in a post–Pan-African extensional environment **(Abdel-Rahman, 2006 ; Be'eri-Shlevin, *et al.*, 2009 and Azer, *et al.*, 2023)**.

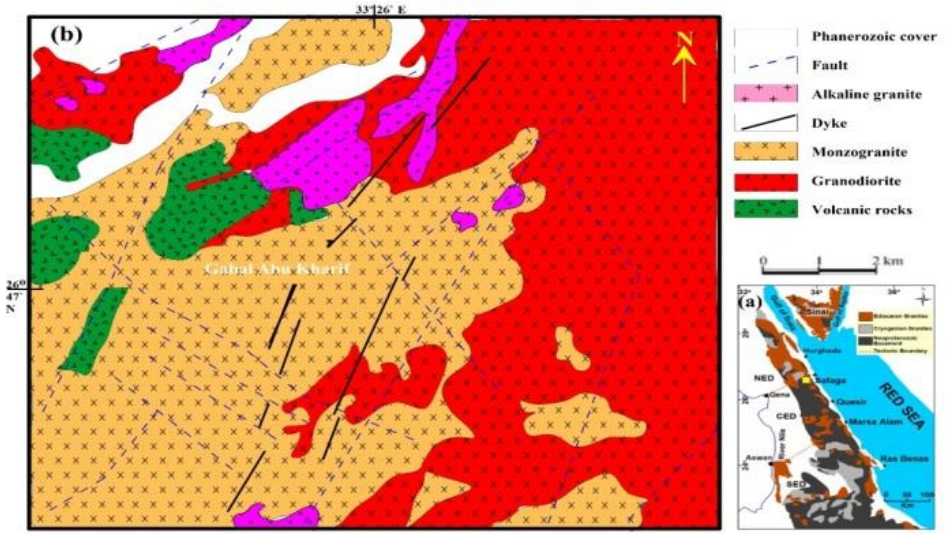

Fig. 1. (a) Location map of the study area; (b) Geological map of the Mount Abu-Kharif area. The map is modified after **Zalata (1972).**

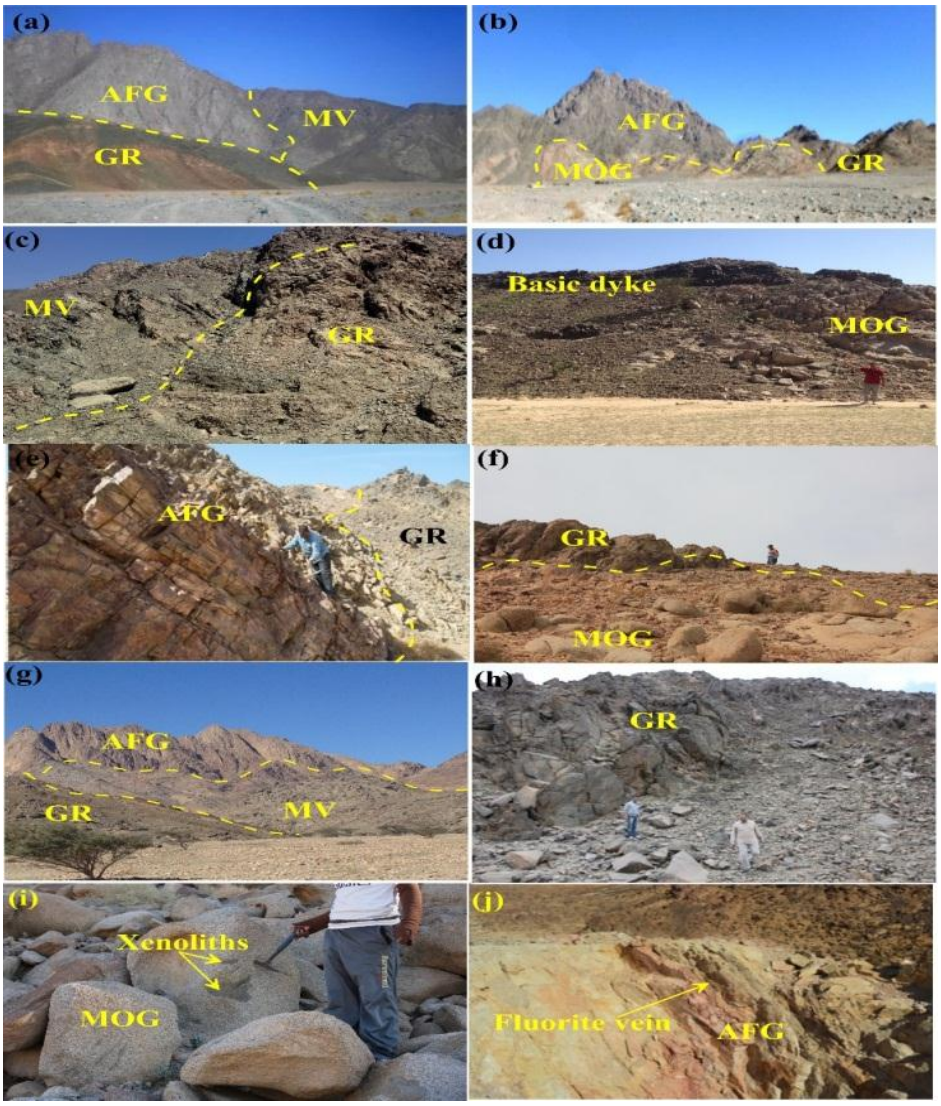

Fig. 2: Field photographs of the of Abu Kharief area (a) Alkali granite (AFG) intruded into both metavolcanics (MV) and granodiorite (GR); (b) Alkali granite cutting both granodiorite and monzogranite (MON); (c) Intrusive contact between granodiorite and metavolcanics; (d) Basic dykes cutting across monzogranite; (e) intrusive contact between highly jointed alkali granite and granodiorite; (f) Monzogranite intruded into granodiorite; (g) Metavolcanic rocks intruded by granodiorite and alkali granite; (h) Exfoliation within granodiorite; (h) Monzogranite envelop undigested massive to irregularly rounded or sub-rounded mafic xenoliths. (i) Mineralized fluorite vein within Alkali granite.

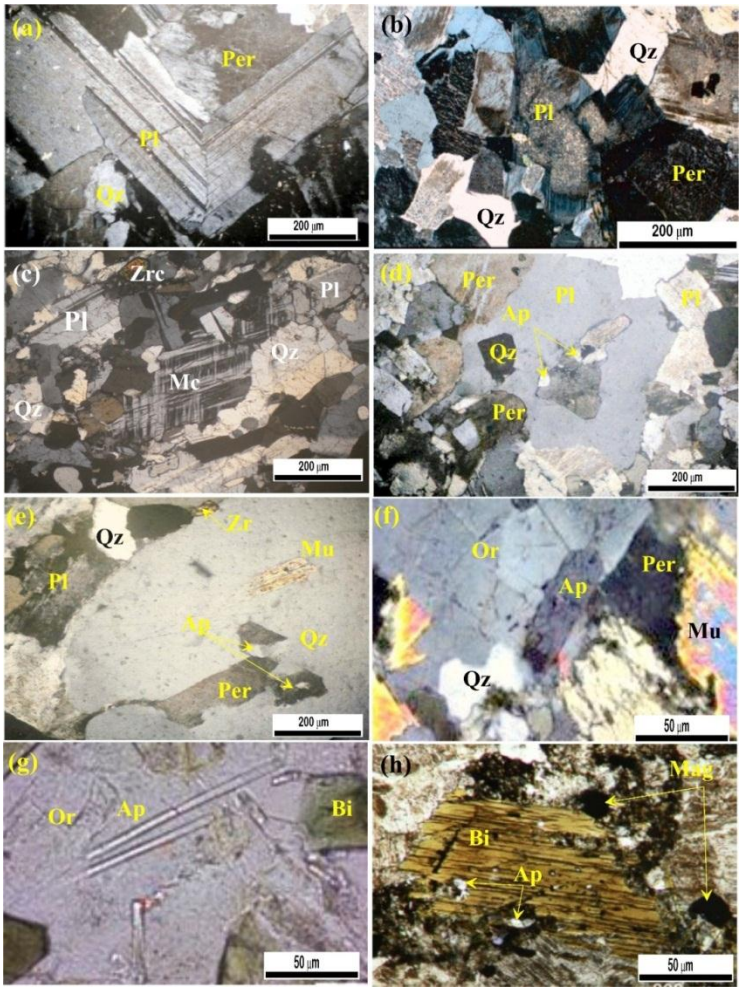

Fig. 3. Petrographical features of Abu Kharief alkali granite showing (a) Unzoned plagioclase crystals in alkali-feldspar granite (AKA); (b) Perthitic orthoclase in AKA; (c) Mineral composition of syenogranite (SG) exhibiting quartz, microcline perthite and zoned plagioclase with accessory zircon grains; (d) AKA exhibiting apatite grains rimmed feldspar grains; (e) Muscovite crystals are occasionally found within plagioclase; (f) Euhedral apatite along the periphery of orthoclase within AKA; (g, h) Acicular apatite associated with biotite in SG. Mineral abbreviations see **(Whitney & Evans, 2010).**

Analytical methods

Major-element analyses of various mineral phases from the Abu Kharif alkali granite were performed using a JEOL JXA-8800 EPMA (20 kV, 20 nA, 3 µm beam) at the Complutense University (ZAF-corrected). Trace and rare-earth elements were measured by LA-ICP-MS (193 nm ArF

laser: MicroLas GeoLas Q-plus + Agilent 7500S) with 60 µm spot sizes; signals under 5× background were treated as below detection **(Morishita *et al.*, 2005)**.

Apatite crystals were hand-picked, separated via heavy-liquid and magnetic methods, mounted in epoxy, and polished to expose core zones. Target spots were selected based on transmitted/reflected light, cathodoluminescence, and BSE imaging. Trace-element data were acquired using a Bruker M90 ICP-MS coupled with a Resonetics RESOlution S-155 laser (6 Hz, 38–60 µm spots, ~6 J/cm²), with He-Ar carrier gas. Each run began with a 20–30 s background followed by 60 s of ablation. Calibration relied on external basaltic glass standards (BCR-2G, BIR-1G, GSE-1G), with no internal standardization **(Liu *et al.*, 2008)**

Twenty-three fresh rock samples were crushed and pulverized via agate mortar for whole-rock geochemical analysis at ACME Analytical Laboratories (Bureau Veritas, Canada). Loss on Ignition (LOI) was calculated from weight loss after igniting each sample at 1000 °C for two hours. Major oxides and select trace elements (Nb, Co, Ni, Sc, Y, Cu, Rb, Sr, Zr) were analyzed by ICP-AES following lithium-borate fusion and nitric acid digestion of 0.2 g sample. Remaining trace and rare-earth elements (REE) were quantified by ICP-MS on the acid digest. Analytical precision and accuracy are ~0.5% for major oxides and better than 8% for trace/REE, based on repeated runs and international reference standards. For full procedural details, see ACME's service descriptions.

Mineral Chemistry

For deeper insights into the mineralogical composition of the AKYG and to infer their petrogenetic characteristics, we conducted detailed analyses of some silicate and non-silicate minerals from both syenogranites (SG) and alkali feldspar granites (AKG) (Supplementary Tables S1-S5), comprising plagioclase and alkali feldspars, biotite, apatite, zircon, as well as iron oxides. This comprehensive approach allows for a nuanced understanding of the magmatic processes and evolutionary history of selected granitic rocks.

Feldspars

To elucidate the mineralogical characteristics of the younger granites at AKYG, we performed electron microprobe analyses (EMPA) on feldspar-group minerals. The structural formulae and end-member compositions (in mole percentages) derived from these analyses are detailed in (Supplementary Table S1).

The obtained alkali Feldspar chemical data distinguished two primary types of K-feldspars: homogeneous varieties (orthoclase/microcline) and perthitic forms, alongside sodic plagioclase. In SG samples, homogeneous K-feldspars exhibited a consistent and elevated K_2O content ranging from 16.11 to 17.11 wt%, corresponding to a high orthoclase component (Or_{94-97})

and a minimal albite component (Ab_{2-4}). Conversely, perthitic K-feldspars displayed a broader K_2O range (5.75—12.28 wt%), resulting in a more variable orthoclase content (33-70 mol%) and higher albite content (28-66 mol%; Supplementary Tables S1).

AKG constitute homogeneous K-feldspars with K_2O contents between 14.12 and 16.57 wt%, with extremely high contents of orthoclase (Or93-98), with low contents of albite (Ab2-7). Additionally, a few perthitic K-feldspars were observed, characterized by orthoclase components of 70–75 mol%, and albite components up to 30 mol% (Fig. 4a).

The analyzed plagioclase of both SG and AKG and alkali feldspar granites are similar and have homogenous composition that are generally restricted to albite (Fig. 4a).

Biotite

The electron microprobe analysis (EMPA) results for biotite samples are compiled in Supplementary Tables S2, with atomic proportions calculated based on an anhydrous total of 22 oxygens. the analysed biotite samples exhibit relatively low concentrations of SiO_2 (33.78-38.97 wt%), Al_2O_3 (9.67-12.39 wt%), FeO (23.10-33.87 wt%), and K_2O (8.27-10.20 wt%). Notably, they are enriched in K2O, Al_2O_3 and FeO while displaying depleted levels of other oxides such CaO. All analyzed biotite samples are nearly identical; however, those from SG exhibit MgO enrichment, while those from AKG show Mg depletion and Fe enrichment (Fig. 4b). The biotite from AG resembles low magnesian biotite and consequently plots near annite, which represents the iron-rich endmember of the biotite group (Fig. 4c). The ternary diagram by **Nachit *et al.*, (2005)** was employed to ascertain the origin of the analyzed biotite samples, revealing that the AKYG biotite samples exhibit a primary magmatic origin (Fig. 4d). Moreover, their chemical compositions are analogous to those of alkali and peralkaline potassic granites (Figs. 4e and f)

Apatite

Acicular apatite grains are recorded in both SG and AFG occur as euhedral to subhedral prismatic crystals, typically 80–250 μm in length and is commonly nestled within K-feldspar and plagioclase phenocrysts (Figs. 3f, g). Most grains exhibit a homogeneous internal texture under BSE imaging (Figs. 5a-d), while fewer crystals display oscillatory zoning—characterized by distinct concentric bands or bright rims; likely resulting from interaction with late-stage hydrothermal fluids that overprint the original magmatic core signatures (Fig. 5e). These zoning patterns are consistent with magmatic-hydrothermal sequences documented in similar granitoids, where it is attributed to interactions with hydrothermal fluids occurring post-apatite crystallization, with bright edges resulting from hydrothermal alteration that obscures the underlying magmatic fingerprints of apatite.

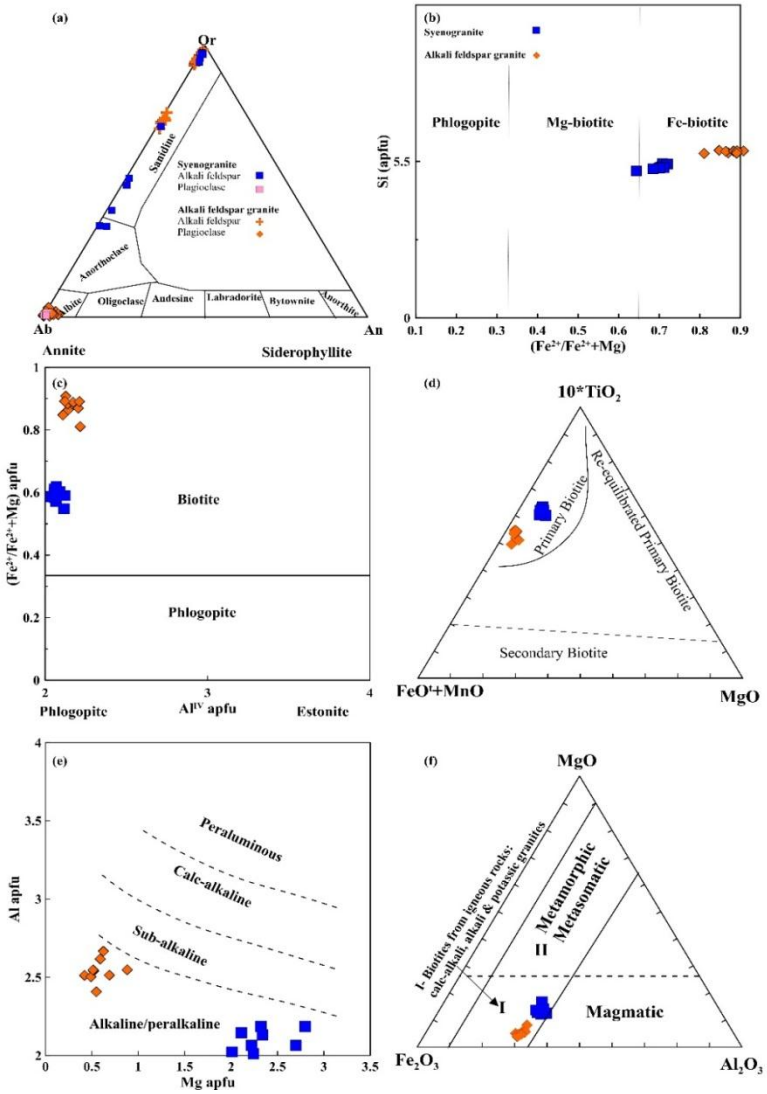

Fig. 4. Mineral chemistry of feldspar and biotite from Abu Kharief alkali granite showing (a) Feldspar classification diagram of the AKAG (Deer, Howie, & Zussman, 1992); (b) Biotite classification scheme for AKAG after (H. Nachit, 1985); (c) Nomenclature scheme of the studied biotite based on the Al (apfu) vs. $Fe^{2+}/(Mg+Fe^{2+})$ diagram of (Deer et al., 1992); (d) (FeO^{t}+ MnO) – 10*TiO_2 – MgO ternary diagram (Hassane Nachit, Ibhi, & Ohoud, 2005) for the classification of AKAG biotite; (e) FeO*vs. Al_2O_3 biotite discriminant diagram (A. M. Abdel-Rahman, 1994) for the analyzed biotite; (f) (FeO^{t}+ MnO) – 10*TiO_2 – MgO ternary diagram (Hassane Nachit et al., 2005) for the classification of AKAG biotite.

Table S1: Electron microprobe analyses of feldspars from Abu Kharief alkali granite.

Rock type	Alkali granite																															
	Alkali feldspar																Plagioclase															
Petro. names	Syenogranite									Alkali feldspar granite							Syenogranite									Alkali Feldspar granite						
Sample No.	SG4/22					SG4/32					AK4/35						SG4/22				SG4/32					AK4/35				AK4/36		
SiO_2	64.40	63.86	63.29	64.20		64.13	63.58	63.75	64.30		63.85	63.75	63.85	63.15	63.79		68.40	67.19	67.58		67.47	67.74	67.82	64.31		67.39	67.99	66.84		67.40	67.02	
TiO_2	0.00	0.01	0.01	0.00		0.01	0.01	0.01	0.00		0.01	0.01	0.01	0.00	0.01		0.01	0.00	0.01		0.01	0.00	0.00	0.02		0.01	0.01	0.01		0.01	0.01	
Al_2O_3	18.68	18.32	18.59	18.21		18.50	18.46	18.40	18.45		18.64	18.40	18.53	19.40	18.60		19.48	18.97	18.60		18.92	19.93	19.56	22.00		18.79	19.04	20.10		19.31	19.66	
FeO*	0.56	0.09	0.09	0.12		0.33	0.09	0.11	0.34		0.33	0.11	0.25	0.26	0.22		0.44	0.65	0.57		0.50	0.40	0.04	0.23		0.61	0.51	0.29		0.47	0.40	
MnO	0.00	0.02	0.00	0.00		0.01	0.01	0.00	0.00		0.00	0.00	0.01	0.01	0.00		0.00	0.00	0.00		0.00	0.00	0.00	0.01		0.00	0.00	0.00		0.00	0.00	
MgO	0.00	0.01	0.00	0.00		0.01	0.01	0.00	0.00		0.00	0.00	0.00	0.00	0.00		0.01	0.00	0.00		0.01	0.00	0.00	0.00		0.00	0.01	0.00		0.00	0.00	
CaO	0.01	0.00	0.00	0.01		0.01	0.00	0.01	0.01		0.01	0.01	0.00	0.01	0.01		0.02	0.00	0.00		0.01	0.00	0.39	3.06		0.00	0.01	0.87		0.29	0.58	
Na_2O	0.69	0.39	0.15	0.68		0.54	0.27	0.42	0.69		0.42	0.42	0.41	0.59	0.47		11.39	11.34	11.26		11.16	11.33	11.23	9.46		11.30	11.33	10.80		11.14	10.96	
K_2O	14.12	16.23	16.57	15.70		16.18	16.40	16.14	15.91		16.35	16.14	15.64	15.35	16.01		0.60	0.20	0.08		0.09	0.22	0.07	0.33		0.14	0.34	0.18		0.22	0.17	
Total	98.46	98.93	98.70	98.92	0.00	99.70	98.82	98.81	99.69	0.00	99.58	98.81	98.70	98.77	99.11		100.35	98.35	98.10		98.17	99.62	99.11	99.42		98.23	99.23	99.08		98.84	98.80	
Cations calculated on basis of 32 oxygens																																
Si	2.99	2.98	2.97	3.00		2.97	2.97	2.98	2.98		0.00	2.98	2.99	2.95	2.97		2.98	2.99	3.02		3.01	2.98	3.00	2.85		3.00	3.00	2.96		2.99	2.98	
Ti	0.00	0.00	0.00	0.00		0.00	0.00	0.00	0.00		1.02	0.00	0.00	0.00	0.00		0.00	0.00	0.00		0.00	0.00	0.00	0.00		0.00	0.00	0.00		0.00	0.00	
Al	0.99	1.01	1.03	1.00		1.01	1.02	1.01	1.01		0.00	1.01	1.02	1.07	1.02		1.00	1.00	0.98		1.00	1.03	1.02	1.12		0.99	0.99	1.05		1.01	1.03	
Cr	0.00	0.00	0.00	0.00		0.00	0.00	0.00	0.00		0.01	0.00	0.00	0.00	0.00		0.00	0.00	0.00		0.00	0.00	0.00	0.00		0.00	0.00	0.00		0.00	0.00	
Fe3	0.02	0.00	0.00	0.00		0.01	0.00	0.00	0.01		0.00	0.00	0.00	0.00	0.01		0.02	0.01	0.00		0.00	0.00	0.00	0.01		0.00	0.00	0.00		0.00	0.00	
Fe2	0.00	0.00	0.00	0.00		0.00	0.00	0.00	0.00		0.00	0.00	0.01	0.01	0.00		0.00	0.02	0.02		0.02	0.01	0.00	0.00		0.02	0.02	0.01		0.02	0.01	
Mn	0.00	0.00	0.00	0.00		0.00	0.00	0.00	0.00		0.00	0.00	0.00	0.00	0.00		0.00	0.00	0.00		0.00	0.00	0.00	0.00		0.00	0.00	0.00		0.00	0.00	
Mg	0.00	0.00	0.00	0.00		0.00	0.00	0.00	0.00		0.00	0.00	0.00	0.00	0.00		0.00	0.00	0.00		0.00	0.00	0.00	0.00		0.00	0.00	0.00		0.00	0.00	
Ca	0.00	0.00	0.00	0.00		0.00	0.00	0.00	0.00		0.00	0.00	0.00	0.00	0.00		0.00	0.00	0.00		0.00	0.00	0.02	0.03		0.00	0.00	0.04		0.01	0.03	
Ba	0.00	0.00	0.00	0.00		0.00	0.00	0.00	0.00		0.04	0.00	0.00	0.00	0.00		0.00	0.00	0.00		0.00	0.00	0.00	0.00		0.00	0.00	0.00		0.00	0.00	
Na	0.76	0.04	0.01	0.06		0.05	0.02	0.04	0.06		0.97	0.04	0.04	0.05	0.04		0.96	0.98	0.98		0.97	0.97	0.96	0.97		0.98	0.97	0.93		0.96	0.94	
K	0.24	0.97	0.99	0.93		0.96	0.98	0.96	0.94		5.00	0.96	0.94	0.92	0.95		0.03	0.01	0.00		0.01	0.01	0.00	0.02		0.01	0.02	0.01		0.01	0.01	
tot. cat.	5.00	5.00	5.00	5.00	0.00	5.00	5.00	5.00	5.00		7.04	5.00	5.00	5.00	5.00		5.00	5.00	5.00		5.00	5.00	5.00	5.00		5.00	5.00	5.00		5.00	5.00	
End Members																																
An	0	0	0	0		0	0	0	0		0	0	0	0	0		0.09	0.00	0.00		0.05	0.00	1.88	3.09		0.00	0.05	4.20		1.41	2.80	
Ab	6.91	3.52	1.36	6.17		4.83	2.44	3.76	6.14		3.76	3.76	3.83	5.49	4.25		96.56	98.85	99.53		99.42	98.74	97.72	95.11		99.19	98.02	94.78		97.33	96.25	
Or	93.04	96.48	98.64	93.78		95.15	97.56	96.21	93.81		96.22	96.21	96.15	94.48	95.73		3.35	1.15	0.47		0.53	1.26	0.40	1.80		0.81	1.94	1.03		1.26	0.95	

Data of EPMA of the studied apatite grains with their calculated structural formula as well as their trace element concentrations are compiled in Supplementary Table S3. All the analyzed apatite grains are chemically identical, whereas those from SG possess lower contents of CaO (44.52-52.87 wt.%) and P_2O5 (34.44-39.80) and Cl (0.05-0.8) than those of AKG (53.22-54.63; 40.26-41.75 and 0.04-0.10, respectively; Supplementary Table S3). On the other hand, AKG possess depleted concentrations of F (3.56-4.56 wt.%) than those of SG (3.56-4.92 wt.%). All the spots of the analyzed apatite that possess F>3.76 wt.% are related to slightly dark domain in the BSE (Fig. 5c). Moreover, the analyzed apatite grains are akin to magmatic apatite (Fig. 6a). Consequently, the magmatic origin of the analyzed apatite is confirmed by their relatively high contents of light rare earth elements (LREE) relative to their high rare earth elements (HREE), where their (La/Lu)n is generally > 2.98 (Chen, Bagas, Liao, **Zhang**, & Li, 2019) (Supplementary Table S3; Fig. 6b) and display prominent negative Eu anomaly (Eu/Eu* < 0.17; Supplementary Table S3). In addition, the primitive mantle-normalized multi-element diagram of apatite samples from the studied granitic rock reveals distinctive geochemical signatures indicative of magmatic processes in evolved alkaline systems. The patterns are marked by strong enrichment in large-ion lithophile elements (LILEs) such as Rb, Th, K, and U, reflecting the incompatible nature of these elements during magmatic differentiation. Notably, there is a pronounced negative anomaly in Nb and Ta, a characteristic commonly associated with crustal contamination or subduction-related signatures in granitic systems. The rare earth element (REE) patterns show moderate to strong enrichment in light REEs (LREEs) such as La, Ce, and Pr, coupled with a slight to moderate negative Eu anomaly (Eu/Eu* < 1), which likely reflects plagioclase fractionation during magma evolution. Additionally, the relatively flat HREE patterns and slight depletion in Y suggest absence or minimal involvement of garnet in the residue or crystallization assemblage. These trace element characteristics align with typical signatures of highly evolved A-type granites and the crystallization of apatite under oxidizing conditions **(Belousova, *et al.*, 2002 ; Pan and Fleet, 2002)**.

Magnetite and ilmenite

Ilmenite and magnetite are the principal oxide minerals in the AKAG. Fe–Ti oxide grains are frequently found in association with biotite (Fig. 3h), indicating that both minerals crystallized during the same magmatic stage. These grains ranged from 0.12 to 0.21 mm and exhibited subrounded morphologies. Ilmenite, showing a light gray color, is typically seen cross-cutting and partially dissolving magnetite (Fig. 5f). Major-element analyses for iron-titanium oxides are displayed in Supplementary Fig. S1 as well as in Supplementary Table S4.

Ilmenite analyses reveal high TiO_2, FeO with moderate MnO contents reaching up to 51.27 wt.%, 48.47 wt % and 3.05 wt % respectively—along with low MgO and Al_2O_3 ($\leq$ 2.22 wt % and $\leq$ 0.13 wt %) (Supplementary Table S4). These values closely match the compositional signature typical of A-type granitic rocks (Fig. 5f)

All the analysed magnetite exhibits high contents of TiO_2 relative to Al_2O_3, MgO and MnO (Supplementary Table S4), which indicate magmatic origin. Moreover, both magnetite and ilmenite composition are consistent with those of ANS a-type granite that originate from oxidized magmatic environment.

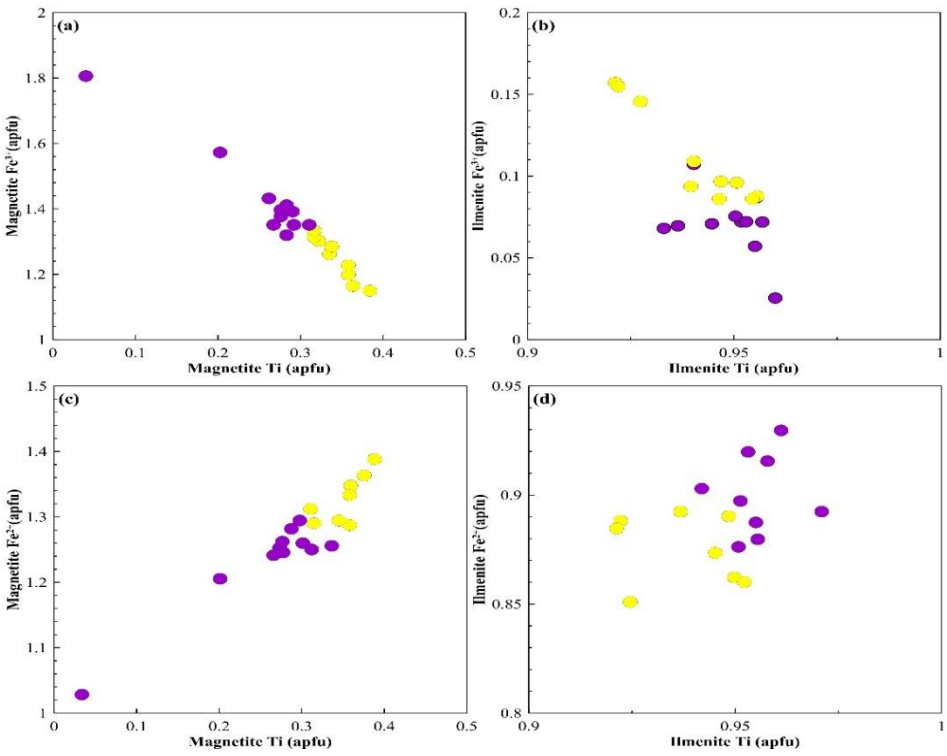

Supplementary Figure S1: Variation diagrams of Ti versus Fe2+ and Fe2+ of the analysed magnetite and ilmenite for AKAG.

Whole rock geochemical data of Abu kharief alkali granites

Whole-rock geochemical analyses of Abu Kahrief alkali granite (AKAG) reveal remarkable compositional homogeneity (Supplementary Table S5). The SiO_2 content is notably high at 71.55-75.58 wt % with the total alkalis (> 7.89 wt %), particularly elevated K_2O (3.81-5.80 wt. %) relative to Na_2O (3.87-4.84 wt. %), which confirm their alkaline affinity. On

comparatively low (Supplementary Table S5). Based on their calculated normative components the AKAG is classified into two groups syenogranite and alkali feldspar granite (Fig. 7a), which is conformable with petrographic observations. Moreover, based on their incompatible elements contents AKAG plot mainly in the field of alkali rhyolite (Fig. 7b), which reflects their relative enrichments of Zr similar to most of the high evolved granitic rocks of the ANS **(Abdelfadil, *et al.*, 2022; Farahat andAzer, 2011 and Sami *et al.*, 2023)**. The AKAG closely resembles the Egyptian "younger" alkali granites (Fig. 7c). The K_2O/Na_2O ratios (0.93-1.26) distinguish AKAG as high-K granites with chemical affinities fluctuating between calc-alkaline to shoshonitic series (Fig. 7d). the relatively low MgO relative to FeO^t content of AKAG yields Mg# values between 2.91 and 26.89 and 12.4, indicating a ferroan A-type granitic affinity (Fig. 7e) **(Frost & Frost, 2011)**.In addition, AKAG constitute Al2O3 ranges from 11.54 to 14.41 wt. %, indicating slightly peraluminous tendencies, where AKAG possess A/CNK values that are generally >1 (Supplementary Table S5) and confirmed by the existence of normative corundum within most of the analysed samples and the presence of primary muscovite in thin sections. Furthermore, AKAG possess high total alkali contents ($K_2O + Na_2O$ = 7.89-10.56 wt. %) which resulted in high agpaitic index for most of the analysed samples (0.79–1.19), evidencing mild alkaline affinity **(Liegeois, *et al.*, 1998)**. Moreover, the normative components of the AKAG pointed to crystallization condition of AKAG melts at 670–800 °C under pressures of 3-5 kb (Fig. 7f).

Chondrite-normalized REE patterns exhibit steep LREE-enriched patterns with $(La/Sm)_n$ = 1.71-4.52, mild HREE depletion $(Gd/Yb)_n$ = 1.34-3.11, and pronounced negative Eu anomalies (Eu/Eu* = 0.09-0.37), characteristic of highly fractionated I- and A-type granites (Fig. 8a). Although HREE contents are lower than LREEs, but the former exceed chondritic values by 5–20 times, implying a garnet-free source **(Dorais & Spencer, 2014).**

Primitive mantle-normalized spider diagrams (Fig. 8b) align the AKAG with typical anorogenic A-type granites **(Whalen, *et al.*, 1987)** particularly of the ANS (Fig. 8b), where it exhibiting enrichments in Rb, Zr, Hf, Th, and U, and negatives for Ba, Nb, Ta, Sr, P, and Ti which is the regarded as the geochemical fingerprints of the ANS A-type granites (**Ali *et al.*, 2012; Sami *et al.*, 2017 and Khedr *et al.*, 2022)**. These geochemical signatures suggest fractionation of plagioclase, apatite or their retention in the residual source. Low Nb/Ta (10.65-11.58) and Zr/Hf (21.17-25.89) ratios are aligned with other highly evolved ANS granites **(Moussa *et al.*, 2021)**. Moreover, the marked P depletion indicates significant apatite removal during AKAG evolution **(Azadbakht, *et al.*, 2018).**

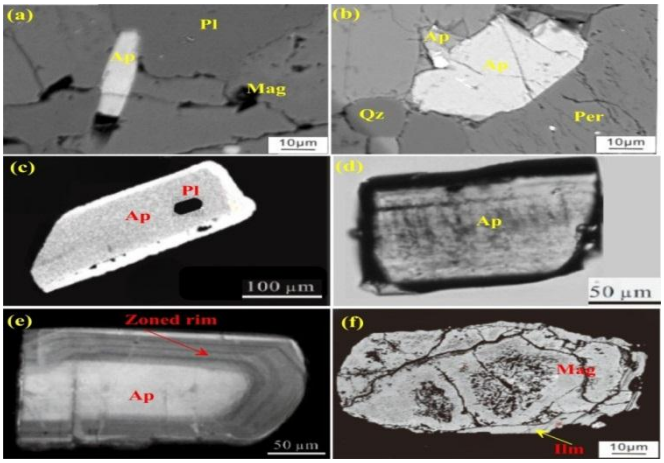

Fig. 5. Representative BSE (Back-scattered electron) image of apatite, magnetite and ilmenite from AKAG showing (a) Acicular apatite homogeneous internal texture in AKA; (b) Euhedral apatite grains along the peripheries of quartz and orthoclase; (c) Plagioclase crystal embedded within apatite grain; (d) Homogenous internal of apatite within SG; (e) Apatite grains display oscillatory zoning characterized by distinct concentric bands or bright rims; (f) Interstitial magnetite and ilmenite formed by ilmenite dissolving the margin of magnetite.

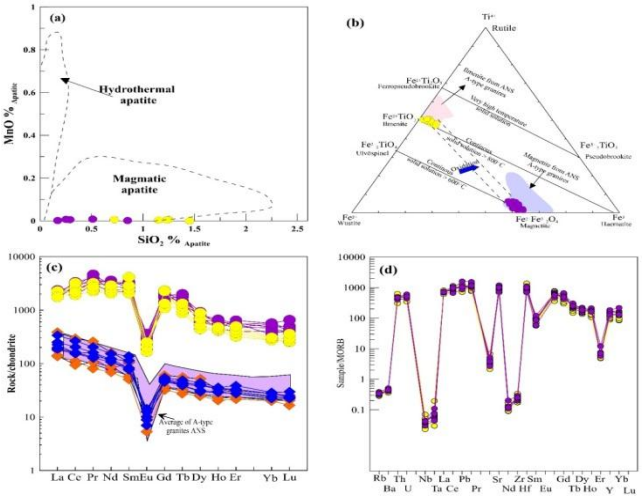

Fig. 6. Mineral chemistry of apatite and iron oxides. (a) Discrimination diagrams of apatite **(Chu *et al.*, 2009)** from AKAG; (b) Ternary plot of cation proportions of Fe2+, Fe3+ and Ti4+ solid system diagram showing the composition and approximate equilibrium tie lines (dashed lines) between analyzed ilmenite and magnetite from EBMU intrusion after **(Buddington & Lindsley, 1964 and Finger *et al.*, 2003)**; Fields of ANS a-type granites are compiled from **(Azer et al., 2023; El-Awady *et al.*, 2024; Elsagheer *et al.*, 2023)** (c) Chondrite-normalized REE patterns and (d) Primitive mantle-normalized spider diagrams of magmatic apatites and whole rock of the AKAG. The chondrite and primitive mantle normalization values are from Salem , **Fasfous, and Abu El-Maaty (1989)**.

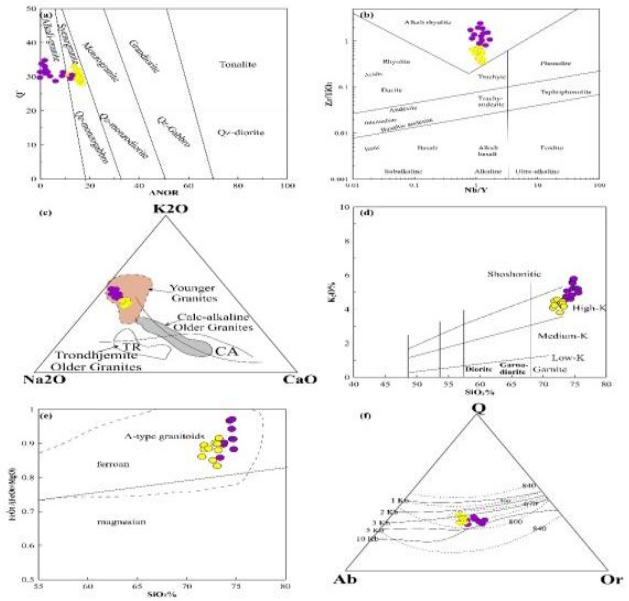

Fig. 7. Geochemical characteristics of AKAG. (a) Q` [100*Q/(Q+Or+Ab+An)] vs. ANOR [100×An/(Or+An)] diagram for normative classification of the studied granitic rocks **(Streckeisen and Le Maitre, 1979);** (b) Zr/TiO_2 vs. Nb/Y classification diagram **(Winchesterand Floyd, 1977)**; (c) Classification diagram of the Egyptian granitic rocks after **(Hassan & Hashad, 1990).** The trondhjemite (TR) and calc-alkaline (CA) trends are from (Barkerand Arth, 1976); d) K_2O vs. SiO_2 variation diagram for the studied granitic rocks. Field are after **(Rickwood, 1989)**; (e) SiO_2 versus FeOt/(FeOt +MgO) variation diagram for SKGG plots fields are after (B. R. Frost et al., 2001); (f) Normative composition of the AKAG plotted in the haplogranite system Q-Ab-Or-H_2O **(Tuttle and Bowen, 1958)**. The dotted line shows the locations of minima melt compositions at saturated water pressures ranging from 0.5 kbar to 10 kbar **(Johannes, 1980).**

RESULTS AND DISCUSSION

Physicochemical conditions during magmatic process

Based on a biotite geothermometer proposed by **Nachit (1985)**, the estimated crystallization temperature for the analysed granite ranges from 753 to 844°C (Supplementary Table S2). Applying the algorithms of **Henry, *et al.*, (2005)**, which based on proportion of Ti within biotite yield estimated temperature of biotite crystallization of the SG ranges from 610 to 650°C, whereas those for AKG give higher value that between 670°C and 700°C (Fig. 8c). Additionally, the whole sum of Al within biotite is regarded as pressure indicator **(Uchida, *et al.*, 2007)** as it is sensitive to pressure changes and tends to rise with increasing formation pressure. Applying the empirical equation of **(Uchida *et al.*, 2007)** on the analysed biotite samples produces a range of crystallization pressures of 1.03-1.08 kbar for SG and 1.08-1.12 kbar for AKG (Supplementary Table S2). Furthermore, the oxygen fugacity (logfO2) could be estimated based on the equation [logfO2= −9.08+5.52×Mg#−9.60×Ti] of

(Uchida *et al.*, 2007). Accordingly, the calculated logfO2 of SG -9.80 and -10.25 and between -11.91 and -12.63 which indicates crystallization from relatively oxidized magma and reflects similarities with the most of the granitic lithologies of the ANS logfO2 =-9.3 to 12 **(Helmy, *et al.*, 2004 and Khedr *et al.*, 2022)**.

For further constrain the melt crystallization conditions, Zr and Hf concentrations in the host granites were used following the model by **(Daneshvar, *et al.*, 2022),** which is suitable for high-silica (SiO_2 > 63 wt.%), metaluminous to peraluminous granites. This Zr–Hf thermometer yields crystallization temperatures ranging from 724°C to 902°C, with an average of ~847 °C. These values are in good agreement with previously reported temperatures for post-collisional granitic intrusions within the ANS (**Azer, *et al.*, 2019 and Sami *et al.*, 2017)**.

The Mn content in apatite can serve as a valuable proxy for assessing the oxygen fugacity ($\log fO_2$) of magmatic systems. Apatite tends to preferentially incorporate Mn^{2+} over its more oxidized forms, Mn^{3+} or Mn^{4+}, under lower oxidation conditions **(Miles *et al.*, 2014)**. Accordingly, **Miles *et al.*, (2014)** introduced an empirical equation to estimate the $\log fO_2$ of silicate melts using Mn concentrations in apatite [$\log fO_2 = -0.0022 \times Mn\ (ppm) \pm 0.0003 - 9.75 \pm 0.46$]. Moreover, apatite is considered as one of the early-magmatic phases in many igneous environments, it often reaches saturation during various stages of magma evolution **(Hoskin, *et al.*, 2000).** To estimate the apatite saturation temperatures (ASTs) of the studied granitic rocks, whole-rock geochemical data were applied to the model developed by **Piccoli and Candela (2002)**. Accordingly, the calculated ASTs of the studied granitic rocks yield limited variation intervals between SG and AKG (768-902°C and 755-86l°C, respectively). The analysed apatite samples are magmatic (Fig. 6a) and they are generally associated with the early forming minerals (Fig. 4). Consequently, the existence of additional Mn-bearing minerals seems improbable to have substantially affected Mn partitioning between apatite and melt. Based on the concentrations of Mn within the analysed apatite (Supplementary Table S3), apatite from syenogranite samples possess higher values (aver. -9.94) magmatic than those calculated for AKG (aver. -11.28), suggesting decline of oxidizing conditions.

REEs of Apatite serves as another valuable mineralogical proxy for assessing magmatic redox conditions, especially through its Eu and Ce anomalies **(Chu *et al.*, 2009; Pan *et al.*, 2016; Xie, *et al.*, 2018 and Tan, *et al.*, 2023)**. In general, apatite that crystallizes from oxidized magma tends to exhibit elevated Eu contents and depleted Ce and Mn concentrations, compared to apatite formed in more reduced magmatic environments (L.-C. Pan et al., 2016**;** Tan et al., 2023). The analysed apatite from the AKG display higher Eu (aver. 0.90) and lower Ce (aver. 12.91) contents (Supplementary Table S3), than those of SG (aver. Eu and Ce are 0.80 and 159.80, respectively), suggesting that the

AKG formed under more oxidizing conditions relative to those of the SG. Furthermore, in the analysed apatite samples display positive correlation between δEu and δCe values (Fig. 8d), supporting crystallization under moderately oxidized conditions **(Pan *et al.*, 2016 and Yang *et al.*, 2020)**.

Thermometric estimates based on coexisting magnetite–ilmenite assemblages **(Andersen, 1985)** suggest equilibrium temperatures ranging from 685–744 °C for SG and 612-680 °C for AKG indicating either late-stage cooling or subsolidus re-equilibration. Oxygen fugacity (log fO_2) values show a systematic variation among lithologies, with higher values in SG (aver. -16.34) than those of AKG (aver. -19.01), suggesting increasing oxidation during magmatic differentiation. The overall trend of the studied granitic rocks reflects decreasing fO_2 with declining temperature (Fig. 8e), likely reflecting cooling-induced re-equilibration (Fig. 8e). Consequently, Ilmenite–magnetite pairs plot between the FMQ (fayalite–magnetite–quartz) and NNO (nickel–nickel oxide) buffers, with most samples clustering near FMQ (Fig. 8e). The trend of Ilmenite-magnetite pairs within the studied granitic rocks (Fig. 8e) reflects temporal variations in the redox state of the granitic magmas, where SG trend shifts from moderately oxidized to slightly oxidized conditions during progressive crystallization to for AKG. This overall decline in log fO_2 values during magma evolution in both granites is likely attributed to extensive fractional crystallization of oxide phases, particularly magnetite, which progressively removes Fe^{3+} from the melt and drives redox changes **(Ghiorso & Evans, 2008)**.

Using the normative data of the studied granitic rocks (Supplementary Table 5), most samples were plotted at the field of granitic rocks, corresponding to pressures that are generally < 5 kbar (Fig. 8f), suggest crystallization under conditions of very low water vapor pressure. These conditions suggest emplacement of water-saturated acidic melts at upper crustal levels. Chemically, the resulting granites are enriched in K_2O but display low contents of MgO, Cr, and Ni (Supplementary Table S5), a geochemical pattern typical of post-collisional granitoids within the ANS **(Azer *et al.*, 2019 and Abdelfadil *et al.*, 2022)**. This signature is commonly linked to magmas associated with extensional tectonics and is often accompanied by enrichment in rare metals such as Nb, Ta, and REEs **(El-Gaby, 2007 and Ali, *et al.*, 2009)**. Moreover, biotite analyses (Supplementary Table S2) show low TiO_2 content, which is consistent with low-pressure emplacement. These findings collectively support that the Abu kharief younger granites solidified at relatively shallow crustal levels **(Bonin, 2007 and Be'eri-Shlevin *et al.*, 2009)**.

It is widely agreed that stated that early-crystallizing phase of apatite could serve as a sensitive monitor of volatile (e.g., Cl and F) behavior and concentrations in magmatic systems **(Webster *et al.*, 2009 and Harlov 2015)**. It is unlikely that the crystallization of biotite or amphibole significantly influenced the partitioning behavior of F and Cl between apatite and melt

(Doherty *et al.,* 2014) . Moreover, F and Cl concentrations of acidic magmas could be traced from the elemental compositions of apatite, where apatite–melt partitioning are used to estimate volatile contents in silicate melts **(Cao *et al.,* 2012)**. The studied granitic rocks possess elevated concentrations F concentrations and high F/Cl ratios (>69), along with low Cl contents (Supplementary Table S3). This suggests that the parent magmas were fluorine-rich and chlorine-poor.

During magma ascent and crystallization, degassing can differentially affect volatile retention, with Cl preferentially partitioning into the vapor phase relative to fluorine **(Stock *et al.,* 2016)**. This process typically results in elevated F/Cl and F/S ratios in the residual melt. Additionally, the exsolution of Cl-bearing magmatic fluids can further increase the F/Cl ratio in apatite formed from the evolving melt **(Keppler, 1996)**. Taken together, the high F/Cl ratios observed in apatite from the studied granitic rocks could be best explained by a combination of an intrinsically high F/Cl ratio in the melt and the effects of fluid exsolution and degassing during late-stage magmatic evolution.

Volatile within AKAG Magma

The F and Cl contents in equilibrium melts of the studied granitic rocks are deduced based on the numerical geodynamic models of **Webster, *et la.*, (2009) and Li & Hermann, (2017),** respectively. Accordingly, the calculated F concentrations in the SG (aver. 1193 ppm), which are slightly lower than those of AKG (aver. 1655; Supplementary Table S3). The estimated Cl contents in equilibrium melts for the studied granitic rocks are relatively low, where the SG samples yield values of the estimated Cl_{melts} (aver. 546 ppm) lower than resulted from AKG samples (aver. 981ppm). Based on these estimates, it is suggested that the parental melts of the studied granitic were likely F- rich and Cl-poor which support the high F/Cl signatures derived from apatite compositions. The marked difference in F and Cl concentrations between the SG and AKG suggests contrasting volatile behaviors during magmatic evolution. In particular, the relatively high F and low Cl contents in both granite types (more pronounced in the AKG) support the interpretation that the magmas were enriched in volatiles but selectively depleted in Cl. This pattern is consistent with magmatic degassing processes, where Cl, being more soluble in aqueous fluids, is preferentially partitioned into a vapor phase during ascent and crystallization, while F remains in the melt. Consequently, the high F/Cl ratios recorded in apatite from both SG and AKG reflect crystallization from residual, Cl-depleted, F-rich melts (Supplementary Table S3).

AKYG is characterized by presence of elevated K_2O (Supplementary Table S5), F-enriched apatite with low Cl concentration (Supplementary Table S3) collectively point to melt-fluid interaction. Such features are characteristic of K- and F-rich granitic systems where volatiles influence the late-stage melt evolution **(Sami, *et al.,* 2022)**. The analysed Apatite from AKYG display Cl depletion and F enrichment, which is indicative for fluorine-

rich evolved systems **(Kieffer *et al.*, 2024)**. In A-type granites, F-rich apatite forms in late magmatic–hydrothermal stages, indicating evolving volatile composition during crystallization. Moreover, Cl depletion in apatite implies low chlorine activity and potential near-isothermal degassing or fluid separation, whereas F enrichment reflects the binding of fluorine in melt, enhancing melt fractionation and lowering melt viscosity, which promotes zircon and accessory phase separation from the melt. Accordingly, the analysed apatite data suggest that AKYG underwent late-stage melt-fluid interaction associated with volatile exsolution during crystallization.

These geochemical features are well-documented in evolved magmatic systems undergoing fluid exsolution and degassing during the late stages of magma evolution (e.g., **Keppler, 1996 and Webster *et al.*, 2009)**.

Petrogenesis of the Abu kharief younger granitic rocks

Granitic typology and alteration of Abu kharief granite

Highly fractionated A-, I-, and S-type granites often exhibit considerable geochemical overlap, making their distinction challenging based solely on major elements **(Chappell, 1999)**. For instance, P content can be a helpful criterion: S-type granites typically show higher P_2O_5 levels (~ 0.14% wt.%), which tend to decline during advanced crystallization **(London, 1992)**. In contrast, the AKAG samples exhibit notably low P_2O_5 concentrations, averaging approximately 0.03%, where their apatite minerals were classified as magmatic (Fig. 6a) which argues against their classification as highly fractionated S-type granites.

The Abu Kharief younger granitic rocks exhibit a geochemical profile consistent with highly evolved, silica-rich magmas. It is enriched in SiO_2 and total alkalis ($K_2O + Na_2O$), while displaying low concentrations of CaO, MgO, P_2O_5, and TiO_2 (Supplementary Table S5), along with a marked negative Eu anomaly, which is typical characterizations of A-type granites **(Whalen *et al.*, 1987 and Bonin, 2007)**. Trace element data reveal enrichments in Rb, Th, U, K, Ta, Nb and Hf, while elements such as Ba, Sr, P, and Ti are notably depleted (Fig. 6a). The marked increase of $(Na_2O + K_2O)/CaO$ ratios (5.98-37.5) and elevated FeO^t/MgO values (2.45-10.06) further align with the characteristics of anorogenic A-type granites **(Frost & Frost, 2011)**.

In addition, Ga concentrations (17.90–29.69 ppm) and 10000*Ga/Al ratios>2.65 (Supplementary Table S5) exceed the lower boundary of 2.6, typically used to classify A-type granites **(Whalen *et al.*, 1987)**. Accordingly, all the analysed samples AKAG are akin to A-type granite (Fig. 8g) and consistent with the trend of highly fractionated A-type granite (**Fig. 8h) (Wu, *et al.*, 2017)**.

Highly fractionated granitic magmas often experience crustal contamination due to their extended crystallization durations, which allow prolonged interaction with surrounding country rocks **(Wu *et al.*, 2017)**. During the early stages of magmatic evolution, assimilation of host rocks is facilitated by high magma temperatures and low viscosity. However, as differentiation

progresses and temperatures drop, the capacity of the residual melt to further assimilate external material diminishes. This late-stage melt, being more viscous and less mobile, commonly traps xenocrysts from the surrounding rocks as it solidifies. Interestingly, the AKYG exhibits only minor xenocrystic content, suggesting that contamination occurred primarily during the initial stages of crystallization, before the magma's assimilation ability declined **(Abdelfadil *et al.*, 2022)**.

The AKYG samples show relatively high Chemical Index of Alteration (CIA) values ranging from 43.33 to 52.27, suggesting minimal post-magmatic alteration and falling within the typical range of fresh felsic rocks (CIA = 45–55) **(Nesbitt & Young, 1982)**. Moreover, their albite-rich plagioclase (Supplementary Table S1) and the overall low CaO content (Supplementary Table S5) might initially suggest potential albite metasomatism **(King, *et al.*, 1997)**, this interpretation is refuted by other geochemical indicators such as their elevated Rb/Sr (>2.56), Rb/Ba (>0.35), K/Ba (>67), and marked negative Eu anomalies (Eu/Eu* < 0.17), all of which point toward significant early fractionation of K-feldspar and plagioclase.

Furthermore, the AKYG display moderate Zr and Hf contents and relatively enriched REE patterns (Figs.8b; Supplementary Table S5), which argue against pervasive albite metasomatism **(Zaraisky, *et al.*, 2009)**. This is further supported by positive correlation between Sr and CaO (Fig. 9a), reinforcing the conclusion that albite metasomatism significantly modified the rock's geochemistry. In addition, compositional data of AKYG possess A/CNK values range between 0.76 and 1.11, while A/NK values vary from 0.81 to 1.31 (Supplementary Table S5), which are consistent with typical A-type granite within ANS (e.g., **Abdel Aal, 1996; Ali *et al.*, 2012; Sami *et al.*, 2018 ; Mahdy *et al.*, 2020 and Feteha *et al.*, 2022)**.

Petrologic consideration and Magmatic source of AKYG

Geochemical Characteristics of AKYG and A-type affinity

Trace element abundances of AKYG are characteristic of highly evolved A-type magmas. The AKYG show elevated concentrations of large-ion lithophile elements (LILEs) such as Rb and Cs, enriched rare earth elements (REEs), and high-field strength elements (HFSEs) including Nb, Ta, Th, U, and Sc. In contrast, elements like Ba, Eu, Sr and Ti are notably depleted (Supplementary Table S5; Fig. 8b). The broad negative correlation observed between Na_2O and K_2O contents (Fig.9b) comparable to low-Ca alkali granites observed in various post-collisional settings (Miller et al., 2007). Most AKYG samples exhibit minimal variation and notably low Nb/Ta (10.65–11.65) and Zr/Hf (21.17-25.87) ratios, aligning closely with those reported for highly evolved granites within the Arabian-Nubian Shield (ANS), such as the Nuweibi, Um Dargag, and Um Maiat bodies (cf. **Moussa *et al.*, 2021**). These geochemical signatures typically reflect advanced magmatic differentiation processes. Moreover, the significant depletion in P (Fig. 8b) further suggests

that accessory mineral fractionation (particularly of apatite) played a key role in magma evolution **(Pichavant *et al.*, 2007 and Jiang *et al.*, 2018)**.

On the Nb–Y–Ce and Nb–Y–3Ga ternary diagrams (Fig. 9c, d), the AKAG samples predominantly plot within the A1-type granite field, closely approaching the transitional boundary with A2-type granites, which suggests a geochemical affinity with within-plate derived magmatic sources. Similarly, data plotted on the Yb/Ta vs. Y/Nb discrimination diagrams (Fig. 9e) reinforce this classification, as the samples continue to cluster near the A1 domain. These trends collectively support an origin linked to anorogenic magmatism, likely associated with extensional tectonic settings, consistent with the petrogenetic characteristics of A-type granites **(Whalen *et al.*, 1987 and Eby, 1992 ;)** and in agreement with the most of the ANS A-type granites of the ANS **(Abdel-Rahman & Martin, 1987; Katzir *et al.*, 2007 and El-Bialy *et al.*, 2020)**.

Magmatic source based on apatite chemistry

Numerous studies have shown that apatite's chemical composition reliably records processes during felsic magma evolution, making it a valuable proxy in petrogenetic investigations **(Xie *et al.*, 2018)**. The analysed apatite samples from both Sg and AKG display similar chondrite and trace elements normalized patterns (Fig. 6), implying they crystallized in comparable sequences. The pronounced negative Eu anomalies observed in both groups are consistent with early feldspar fractionation, particularly plagioclase or lower magmatic oxygen fugacity ($\log fO_2$) conditions **(Ballard, *et al.*, 2002)**. As deduced before that estimated oxygen fugacity of both SG and AKG point to oxidized magma, thus the negative Eu anomalies (Fig. 6) of the analysed apatite are attributed to early plagioclase crystallization, where plagioclase crystals were enclosed within apatite grains (Fig. 5c). Plagioclase efficiently removes Eu and Sr from the melt, and hence they followed apatite will be depleted in both Sr and Eu (Fig. 6). Such patterns strongly point to a fractionation-controlled evolution, where plagioclase crystallized prior to apatite.

The Sr contents of the analysed apatite from SG and AKG decrease with increasing of δEu, whereas Y contents increase (Fig. 9fa, g), which suggest progressive fractionation in the AKAG suites. Moreover, SG apatite possesses higher Sr and lower Y than those of AKG, suggesting that the two groups experienced differing degrees of early magmatic fractionation.

The apatite composition of granitic rocks could be used to record the sequence of mineral growth within evolving magmas (**Pan *et al.*, 2016**). Accordingly, based on the correlation normalized REE ratios (La/Yb)n and (La/Sm)n against Sr concentration of apatite (Fig. 10a, b); which exhibit abrupt decrease of REEs normalized ratio with limited variation within Sr contents, implying that plagioclase crystallization dominated the early magmatic differentiation and indicating that LREE enrichment and HREE depletion are linked to Cl-rich fluid exsolution during magmatic evolution **(Keppler, 1996)**.

Table S2: Electron microprobe analyses of Biotite from Abu Kharief alkali granite.

Mineral	Biotite								Biotite								
Rock type	Syenogranite								Alkali feldspar granite								
Sample	SG4/22		SG4/32			SG4/33			AK4/35		AK4/36			AK4/37			
SiO_2	34.20	34.58	33.97	34.41	34.97	33.08	33.85	33.49	36.16	36.64	36.31	36.95	36.21	35.84	36.17	36.87	35.78	35.97
TiO_2	2.27	2.28	2.25	2.21	2.20	1.94	2.31	2.32	3.36	3.39	3.28	3.17	3.45	3.39	3.29	3.35	3.34	3.34
Al_2O_3	15.67	14.22	14.99	15.07	15.00	14.30	14.27	14.91	13.52	13.27	13.91	14.27	13.15	12.49	13.39	13.32	13.36	13.39
FeO	29.10	28.87	29.55	29.79	29.00	29.30	30.17	28.39	28.14	28.49	29.50	29.86	30.48	30.21	30.65	30.15	30.87	29.53
MnO	0.04	0.16	0.31	0.66	0.37	0.36	0.54	0.74	0.33	0.45	0.24	0.31	0.57	0.67	0.51	0.55	0.54	0.58
MgO	5.82	5.98	8.25	6.37	5.68	5.98	6.53	6.55	3.69	2.87	2.48	2.64	1.74	2.25	2.16	2.06	2.12	2.09
CaO	0.08	0.05	0.06	0.07	0.07	0.09	0.05	0.04	0.56	0.54	0.22	0.25	0.02	0.02	0.05	0.04	0.02	0.02
Na_2O	0.27	0.13	0.23	0.23	0.15	0.22	0.22	0.29	0.39	0.37	0.28	0.14	0.14	0.24	0.09	0.20	0.19	0.09
K_2O	8.20	8.13	7.86	7.78	8.16	8.64	7.82	7.90	9.46	8.78	9.16	8.27	8.35	8.55	8.48	9.28	8.41	10.51
Total	95.66	94.41	97.48	96.60	95.61	93.92	95.77	94.64	95.61	94.80	95.38	95.86	94.10	93.65	94.79		94.65	95.52
Cations based on 22 oxygens																		
Si	5.45	5.58	5.32	5.44	5.57	5.43	5.43	5.40	5.78	5.83	5.83	5.86	5.91	5.90	5.86	5.91	5.82	5.83
Al^{IV}	2.55	2.42	2.68	2.56	2.43	2.57	2.57	2.60	2.22	2.17	2.17	2.14	2.09	2.10	2.14	2.09	2.18	2.17
Al^{VI}	0.39	0.29	0.09	0.26	0.38	0.20	0.13	0.24	0.33	0.46	0.46	0.53	0.43	0.32	0.42	0.43	0.38	0.39
Ti	0.27	0.28	0.27	0.26	0.26	0.24	0.28	0.28	0.40	0.40	0.40	0.38	0.42	0.42	0.40	0.40	0.41	0.41
Fe^{2+}	3.88	3.90	3.87	3.94	3.86	4.03	4.05	3.83	3.76	3.96	3.96	3.96	4.16	4.16	4.15	4.04	4.20	4.00
Mn	0.01	0.02	0.04	0.09	0.05	0.05	0.07	0.10	0.04	0.03	0.03	0.04	0.08	0.09	0.07	0.07	0.07	0.08
Mg	1.38	1.44	1.93	1.50	1.35	1.47	1.56	1.58	0.88	0.59	0.59	0.62	0.42	0.55	0.52	0.49	0.52	0.50
Ca	0.01	0.01	0.01	0.01	0.01	0.02	0.01	0.01	0.10	0.04	0.04	0.04	0.00	0.00	0.01	0.01	0.00	0.00
Na	0.08	0.04	0.07	0.07	0.04	0.07	0.07	0.09	0.12	0.09	0.09	0.04	0.04	0.08	0.03	0.06	0.06	0.03
K	1.67	1.67	1.57	1.57	1.66	1.81	1.60	1.63	1.93	1.87	1.87	1.67	1.74	1.79	1.75	1.90	1.75	2.17
Total	15.69	15.65	15.85	15.71	15.62	15.88	15.77	15.75	15.57	15.44	15.44	15.29	15.30	15.41	15.35		15.39	15.59
Mg#	0.36	0.37	0.50	0.38	0.35	0.36	0.39	0.41	0.23	0.15	0.15	0.16	0.10	0.13	0.13		0.12	0.13
Al^{Total}	2.94	2.70	2.77	2.81	2.81	2.77	2.70	2.84	2.55	2.63	2.63	2.67	2.53	2.42	2.56		2.56	2.56

Table S3: Electron microprobe analyses and trace and rare elements contents of apatite from Abu Kharief alkali granite

Mineral	Apatite						Apatite					
Rock type	Syenogranite						Alkali feldspar granite					
Sample	SG4/22		SG4/32				AK4/35		AK4/36			
SiO2	0.72	1.25	1.45	1.23	1.15		0.85	0.51	0.29	0.25	0.17	0.71
TiO2	0.02	0.00	0.04	0.00	0.03		0.03	0.10	0.01	0.02	0.09	0.12
TFeO	0.14	0.12	0.11	0.19	0.19		0.12	0.09	0.02	0.04	0.02	0.08
MnO	0.01	0.01	0.01	0.01	0.02		0.07	0.11	0.10	0.14	0.13	0.37
MgO	0.03	0.08	0.04	0.01	0.02		0.03	0.02	0.03	0.02	0.03	0.08
CaO	44.52	51.68	52.14	52.80	52.87		53.22	53.94	54.21	54.44	54.63	163.29
Na2O	0.07	0.05	0.03	0.06	0.05		0.05	0.07	0.02	0.03	0.02	0.07
P2O5	34.44	38.56	38.84	39.80	39.70		40.26	41.38	41.51	41.75	41.50	124.75
F	3.92	3.56	4.20	4.56	4.25		3.76	3.68	3.56	3.90	3.58	11.05
Cl	0.08	0.06	0.05	0.05	0.05		0.10	0.06	0.09	0.04	0.04	0.17
												0.00
Si	0.09	0.13	0.15	0.12	0.12		0.09	0.05	0.03	0.03	0.02	0.07
Ti	0.00	0.00	0.00	0.00	0.00		0.00	0.01	0.00	0.00	0.01	0.01
Fe+2	0.01	0.01	0.01	0.02	0.02		0.01	0.01	0.00	0.00	0.00	0.01
Mn	0.01	0.01	0.00	0.00	0.00		0.00	0.01	0.01	0.01	0.00	0.01
Mg	0.01	0.01	0.01	0.00	0.00		0.00	0.00	0.00	0.00	0.00	0.01
Ca	5.79	5.71	5.68	5.72	5.73		5.80	5.86	5.93	5.93	5.94	17.80
Na	0.02	0.01	0.01	0.01	0.01		0.01	0.01	0.00	0.01	0.00	0.01
P	0.71	0.67	0.67	0.68	0.68		0.69	0.71	0.72	0.72	0.71	2.15
F	1.51	1.16	1.35	1.46	1.36		1.21	1.18	1.15	1.26	1.15	3.56
Cl	0.02	0.01	0.01	0.01	0.01		0.02	0.01	0.02	0.01	0.01	0.03
Volatile in melts												
F/Cl	48.17	57.99	81.69	88.69	82.66		37.10	59.94	38.97	0.01	0.01	38.99
Fmelt (ppm)	1141.00	1036.00	1223.00	1327.00	1237.00		1096.00	1072.00	1036.00	1702.00	3368.00	6106.00
Kd(Cl-OH)	5.97	6.28	5.98	5.94	5.93		10.74	7.85	13.27	256.00	428.00	697.27
Cl melt (ppm)	553.00	593.00	542.00	500.00	542.00		568.00	600.00	590.00	1280.00	1866.00	3736.00
Apattite trace Elements												
La	459.33	492.56	536.77	415.87	560.35		415.87	475.94	514.66	476.32	470.98	463.29
Ce	1175.24	1624.78	1336.99	1974.52	1428.22		1624.78	2042.34	1911.88	1523.33	1678.01	1175.24
Pr	209.03	223.30	298.92	254.03	319.31		363.26	375.73	298.92	280.25	427.45	280.25
Nd	934.51	1029.40	1172.87	1336.34	1572.47		1425.33	1099.64	1623.99	1425.33	1336.34	1011.34
Sm	307.32	361.63	425.53	613.19	443.54		461.60	347.48	376.93	500.72	361.63	322.80
Eu	9.42	11.53	14.14	14.14	12.02		14.72	17.32	14.72	16.64	20.38	9.81
Gd	467.22	448.25	215.87	264.35	337.43		366.03	448.25	413.22	337.43	381.52	286.76
Tb	31.98	36.10	42.48	47.96	54.22		72.03	52.02	46.08	63.80	69.21	72.03
Dy	109.04	128.31	170.71	217.91	200.88		177.66	145.08	200.88	226.78	157.37	157.37
Ho	22.35	22.35	24.21	26.26	32.21		25.23	36.36	36.36	29.69	25.23	33.52
Er	51.30	60.37	68.15	80.19	90.53		62.82	76.93	90.53	76.93	102.36	86.99
Yb	43.87	43.87	47.59	49.53	56.00		65.89	74.39	77.42	87.53	91.09	91.09
Lu	6.18	6.43	7.27	8.90	10.90		9.28	9.28	12.33	10.07	11.02	16.13
Rb	0.18	0.19	0.21	0.23	0.23		0.25	0.18	0.20	0.22	0.24	0.20
Ba	2.54	3.08	3.21	2.82	3.35		3.35	2.81	3.14	3.02	3.58	2.83
Th	34.20	39.76	45.23	25.94	38.08		53.57	36.98	42.49	35.58	42.65	34.21
U	9.21	11.67	11.17	7.29	12.18		12.18	10.44	11.42	9.23	12.71	9.31
Nb	0.02	0.03	0.04	0.02	0.05		0.02	0.02	0.03	0.03	0.03	0.02
Ta	0.00	0.00	0.00	0.00	0.01		0.00	0.00	0.00	0.00	0.00	0.00
Pb	58.23	72.86	64.22	86.53	90.33		88.46	50.55	68.54	75.38	114.40	61.10
Sr	60.74	69.28	75.50	143.48	45.20		85.89	65.01	72.39	109.49	55.88	92.20
Zr	1.01	1.06	1.55	1.31	1.06		1.84	1.03	1.31	1.43	2.28	1.21
Hf	0.05	0.05	0.07	0.08	0.09		0.11	0.05	0.06	0.07	0.09	0.07
Y	24.62	33.63	30.94	21.94	56.17		22.90	29.12	32.28	26.44	54.99	26.28

Table S4: Electron microprobe analyses of Fe-Ti oxides from the Abu Kharief alkali granites.

Rock type	Syenogranite								Alkali feldspar granites											
Mineral	Ilmenite		Magnetite		Ilmenite		Magnetite		Ilmenite		Magnetite		Ilmenite		Magnetite		Ilmenite		Magnetite	
Sample No.	SG4/22		SG4/22		SG4/32		SG4/32		AK4/35		AK4/35		AK4/35		AK4/35		AK4/36		AK4/36	
SiO_2	0.25	0.03	0.31	0.07	0.33	0.04	0.31	0.07	0.71	0.04	0.12	0.04	0.43	0.00	0.08	0.06	0.04	0.09	0.04	0.16
TiO_2	11.22	50.22	10.22	49.87	13.87	51.23	10.54	50.14	11.98	49.97	9.21	49.21	7.29	51.27	4.95	47.02	3.27	45.26	3.27	45.11
Al_2O_3	0.46	0.00	0.49	0.00	0.48	0.00	0.36	0.08	0.56	0.00	0.45	0.03	0.34	0.00	0.27	0.00	3.16	0.02	3.16	0.12
Fe2O3(T)															0.00	0.00	0.00	0.00	0.00	0.00
FeO[t]	75.12	46.64	75.67	44.37	70.21	42.24	77.42	46.94	76.21	44.37	79.67	44.22	79.31	45.79	80.93	48.47	79.84	45.06	79.84	44.44
MnO	0.62	1.22	0.23	1.12	0.19	1.31	0.57	1.22	0.15	1.51	0.22	1.08	0.21	1.03	0.04	1.35	0.36	1.18	0.36	2.17
MgO	0.06	0.03	0.01	0.00	0.01	0.00	0.00	0.00	0.20	0.00	0.00	0.00	0.50	0.00	0.06	0.34	0.04	0.19	0.04	0.03
CaO	0.08	0.04	0.04	0.03	0.07	0.02	0.00	0.05	0.11	0.00	0.00	0.00	0.03	0.00	0.00	0.00	0.00	0.00	0.00	0.00
Na_2O	0.12	0.03	0.03	0.07	0.12	0.18	0.14	0.00	0.13	0.19	0.08	0.19	0.05	0.00	0.00	0.00	0.00	0.00	0.00	0.00
K_2O	0.03	0.00	0.00	0.00	0.00	0.00	0.03	0.03	0.00	0.00	0.00	0.08	0.00	0.00	0.00	0.00	0.00	0.00	0.00	0.00
Cr2O3	0.02	0.03	0.05	0.00	0.00	0.04	0.02	0.02		0.00	0.07	0.04	0.04	0.08	0.01	0.06	0.68	0.06	0.68	0.06
BaO	0.00	0.00	0.00	0.00	0.00	0.00	0.00	0.04	0.00	0.00	0.00	0.00	0.00	0.00	0.00	0.00	0.00	0.00	0.00	0.00
ZnO	2.31	0.71	0.87	2.36	2.27	3.47	1.88	0.41	0.91	3.03	0.71	2.63	0.86	0.61	0.03	0.00	0.19	0.00	0.19	0.00
V2O3	0.19	0.06	0.06	0.18	0.17	0.14	0.03	0.12	0.02	0.14	0.34	0.14	0.09	0.12	0.51	2.87	0.36	2.26	0.58	2.11
NiO	0.00	0.00	0.02	0.00	0.00	0.00	0.00	0.00	0.00	0.00	0.08	0.00	0.01	0.00	0.09	0.05	0.12	0.07	0.12	0.07
Total	90.48	99.01	## 88.00	98.07	## 87.72	98.67	## 91.30	99.12	## 90.98	99.25	## 90.95	97.66	## 89.16	98.90	## 86.97	100.23	88.07	94.20	## 88.29	94.25
Formula based on 4 cations and 6 oxygen atoms																				
Si	0.00	0.00	0.00	0.00	0.00	0.00	0.01	0.01	0.00	0.00	0.00	0.01	0.00	0.00	0.01	0.00	0.00	0.00	0.00	0.00
Ti	0.92	0.90	0.11	0.11	0.90	0.89	0.06	0.05	0.90	0.89	0.16	0.07	0.88	0.88	0.07	0.15	0.91	0.90	0.10	0.10
Al	0.00	0.00	0.02	0.02	0.00	0.00	0.12	0.22	0.00	0.00	0.01	0.12	0.00	0.00	0.10	0.01	0.00	0.00	0.15	0.15
Fe3+	0.12	0.13	1.71	1.70	0.14	0.15	1.74	1.65	0.14	0.15	1.64	1.69	0.17	0.17	1.72	1.65	0.13	0.13	1.61	1.61
Fe2+	0.82	0.84	1.06	1.06	0.80	0.83	1.00	0.98	0.80	0.83	1.15	1.06	0.83	0.84	1.07	1.15	0.88	0.86	1.08	1.08
Mn	0.06	0.03	0.02	0.02	0.01	0.01	0.04	0.05	0.01	0.01	0.00	0.01	0.02	0.03	0.00	0.00	0.03	0.05	0.01	0.01
Mg	0.03	0.03	0.03	0.03	0.08	0.05	0.02	0.02	0.08	0.05	0.01	0.00	0.02	0.01	0.00	0.00	0.01	0.00	0.00	0.00
Ca	0.00	0.00	0.00	0.00	0.00	0.00	0.00	0.00	0.00	0.00	0.00	0.00	0.00	0.00	0.00	0.00	0.00	0.00	0.00	0.00
Na	0.00	0.00	0.00	0.00	0.00	0.00	0.00	0.00	0.00	0.00	0.00	0.00	0.00	0.00	0.00	0.00	0.00	0.00	0.00	0.00
K	0.00	0.00	0.00	0.00	0.00	0.00	0.00	0.00	0.00	0.00	0.00	0.00	0.00	0.00	0.00	0.00	0.00	0.00	0.00	0.00
Cr	0.00	0.00	0.04	0.04	0.00	0.00	0.01	0.01	0.00	0.00	0.00	0.03	0.00	0.00	0.02	0.00	0.00	0.00	0.02	0.02
Ba	0.00	0.00	0.00	0.00	0.00	0.00	0.00	0.00	0.00	0.00	0.00	0.00	0.00	0.00	0.00	0.00	0.00	0.00	0.00	0.00
Zn	0.00	0.00	0.00	0.00	0.00	0.00	0.00	0.00	0.00	0.00	0.00	0.00	0.00	0.00	0.00	0.00	0.00	0.00	0.01	0.01
V	0.04	0.06	0.01	0.02	0.05	0.06	0.00	0.01	0.05	0.06	0.01	0.01	0.07	0.06	0.01	0.02	0.05	0.05	0.01	0.02
Ni	0.00	0.00	0.01	0.01	0.00	0.00	0.00	0.00	0.00	0.00	0.01	0.00	0.00	0.00	0.00	0.00	0.00	0.00	0.00	0.00
Total	4.00	4.00	4.00	4.00	4.00	4.00	4.00	4.00	4.00	4.00	4.00	4.00	4.00	4.00	4.00	4.00	4.00	4.00	4.00	4.00
Mole% of Ilmenite	93.29%	93.21%			92.24%	91.92%			92.24%	91.92%			91.01%	91.09%			93.27%	93.04%		
Mole% of ulvöspinel			4.24%	4.93%			5.06%	4.46%			4.63%	5.00%			5.84%	5.74%			5.76%	5.78%
Temp (°C)	730.98	752.26	730.98	752.26	699.27	708.14	699.27	708.14	689.39	699.17	689.39	699.17	672.41	688.79	672.41	688.79	670.58	672.41	670.58	672.41
*$\log_{10}$ fO2	-14.88194	-15.61038	-14.88194	-15.61038	-14.88194	-15.61038	-14.88194	-15.61038	-16.47713	-16.68675	-16.47713	-16.68675	-16.91349	-17.44549	-16.91349	-17.44549	-18.03619	-18.24003	-18.24003	-18.27255

Table S5: Major (wt.%), trace elements (ppm) compositions and petrochemical parameters for the Abu Kharief

Rock type	Syenogranite										Alkali feldspar granite												
Sample	SG4/22	SG4/32	SG4/33	SG4/34	SG4/35	SG4/36	SG4/37	SG4/38	SG4/39	SG4/40	AK4/35	AK4/36	AK4/37	AK4/38	AK4/39	AK4/40	AK4/41	AK4/42	AK4/43	AK4/44	AK4/45	AK4/46	AK4/47
Major element (wt.%)																							
SiO_2	71.55	71.77	71.78	72.20	72.65	72.86	73.09	73.12	73.19	73.28	73.38	73.71	73.79	74.35	74.56	74.59	74.63	74.70	74.76	74.84	75.27	75.55	75.58
TiO_2	0.35	0.31	0.28	0.31	0.33	0.27	0.25	0.28	0.32	0.35	0.25	0.23	0.26	0.21	0.20	0.21	0.20	0.22	0.20	0.23	0.20	0.19	0.21
Al_2O_3	14.41	14.13	13.99	13.97	14.03	12.42	13.62	13.45	13.33	12.69	13.72	13.57	13.36	13.25	12.19	11.95	12.00	12.49	12.01	11.76	11.82	11.86	11.54
FeO*	2.09	2.52	2.49	2.37	1.89	2.54	1.75	2.37	2.04	2.57	1.68	1.34	1.09	1.54	2.04	1.38	1.28	1.37	1.21	1.54	1.36	1.15	1.31
MnO	0.07	0.07	0.07	0.06	0.06	0.07	0.05	0.06	0.06	0.05	0.04	0.05	0.06	0.05	0.05	0.04	0.04	0.05	0.05	0.04	0.04	0.04	0.03
MgO	0.34	0.30	0.33	0.31	0.33	0.28	0.35	0.27	0.28	0.24	0.28	0.15	0.12	0.05	0.12	0.04	0.12	0.13	0.16	0.16	0.12	0.42	0.13
CaO	1.35	1.29	1.37	1.21	1.17	1.31	1.13	1.01	0.93	0.95	0.85	0.81	0.75	0.66	0.62	0.70	0.62	0.46	0.28	0.28	0.46	0.50	0.42
Na_2O	3.97	4.15	4.33	4.13	4.08	4.19	4.24	4.07	4.02	4.01	4.17	4.39	4.31	4.41	4.28	4.79	4.84	4.15	4.82	4.75	4.53	4.38	4.59
K_2O	4.09	4.48	4.23	4.57	3.81	4.39	4.46	4.34	4.17	4.17	4.56	4.60	5.08	4.61	4.84	5.58	5.53	5.23	5.74	5.80	5.23	5.19	4.98
P_2O_5	0.02	0.02	0.02	0.02	0.02	0.02	0.02	0.02	0.02	0.02	0.01	0.01	0.01	0.01	0.01	0.01	0.01	0.01	0.01	0.01	0.01	0.01	0.01
L.O.I	0.72	0.58	0.91	0.59	0.96	0.96	0.59	0.70	0.73	0.97	0.58	0.53	0.52	0.54	0.37	0.45	0.44	0.42	0.37	0.48	0.37	0.60	0.42
Total	98.96	99.61	99.80	99.74	99.33	99.30	99.55	99.68	99.08	99.29	99.53	99.40	99.36	99.69	99.28	99.74		99.22	99.62	99.90	99.40		99.23
Na_2O+K_2O	8.06	8.63	8.56	8.70	7.89	8.58	8.70	8.41	8.19	8.18	8.73	8.99	9.39	9.02	9.12	10.37		9.38	10.56	10.55	9.76	9.56	9.57
Trace element (*ppm*)																							
V	15.60	14.13	11.71	15.29	9.48	12.39	10.21	14.86	12.68	15.56	13.06	11.66	17.30	15.83	13.41	16.99	11.18	14.09	11.91	16.56	14.38	17.26	14.76
Cr	11.50	10.74	10.41	11.61	10.41	9.65	11.61	8.99	10.08	8.45	10.52	8.34	7.24	7.79	7.03	6.48	6.26	9.10	9.32	8.12	8.88	7.90	9.76
Co	18.83	15.19	19.56	20.65	14.83	13.02	10.10	17.75	14.46	5.73	3.19	9.73	3.19	4.65	11.56	11.19	7.19	9.38	10.46	6.46	6.46	3.56	2.83
Ni	17.31	14.76	12.40	13.31	16.21	14.94	13.67	17.86	14.58	13.49	12.03	9.48	11.31	7.48	8.94	12.03	9.48	7.13	5.67	6.76	6.58	14.03	6.21
Cu	2.13	1.08	1.36	1.59	0.91	1.23	0.91	0.89	0.94	1.02	1.06	1.25	2.70	2.78	3.06	3.29	2.61	3.28	2.54	3.18	2.26	2.18	2.26
Zn	9.51	11.36	26.24	17.19	7.88	7.44	8.72	10.26	10.75	24.46	8.42	10.00	13.06	27.94	18.89	9.58	9.14	10.42	11.96	12.45	26.16	10.12	11.70
Cs	0.57	0.88	0.30	0.95	1.05	0.95	1.88	1.04	0.95	0.20	1.21	0.82	1.02	1.58	1.19	0.57	2.02	0.42	0.53	2.11	1.44	1.14	2.02
Rb	52.13	53.03	54.71	56.40	57.52	56.29	58.19	59.75	59.75	60.77	61.33	63.79	64.91	63.79	66.37	67.26	67.83	69.40	71.41	72.09	73.76	70.74	68.61
Ba	353.21	312.83	311.94	219.24	288.95	278.92	265.97	242.10	277.02	290.86	284.38	277.02	253.14	236.63	232.06	252.25	242.10	252.25	224.70	199.05	220.13	232.95	204.51
Th	71.28	70.24	69.62	69.83	70.79	69.62	71.13	73.27	68.79	67.83	68.17	70.79	70.17	68.66	71.00	72.71	72.86	68.25	66.25	67.42	67.97	67.14	65.01
U	36.27	36.32	36.32	36.45	36.51	36.02	38.38	37.35	37.35	35.49	36.88	35.50	37.06	35.85	36.86	37.06	36.61	38.27	34.98	36.95	36.09	36.78	35.40
Nb	486.75	484.67	480.83	482.23	476.66	477.35	472.13	478.05	470.04	470.74	468.29	468.29	474.91	462.72	461.67	458.90	455.76	454.01	459.25	453.33	450.19	457.85	448.79
Ta	44.24	44.24	43.61	43.73	43.23	43.10	42.84	43.23	43.35	42.27	43.99	42.08	41.06	42.34	40.81	40.87	40.11	41.76	40.36	39.28	41.19	40.49	38.77
Pb	52.81	49.85	50.14	55.00	61.92	57.16	60.68	74.68	77.97	52.04	47.14	67.38	58.33	64.26	67.38	72.26	44.13	51.69	45.97	61.23	58.37	47.03	64.26
Sr	22.68	20.16	22.05	18.25	16.98	19.52	16.35	14.78	16.03	11.92	8.76	16.67	17.62	10.97	11.60	7.49	10.02	11.92	10.65	6.54	6.22	6.22	8.76
Zr	117.33	132.89	149.89	136.22	167.56	186.44	192.67	196.78	198.22	206.44	234.67	237.33	264.67	288.67	315.78	348.89	339.56	366.44	359.56	377.78	399.78	431.11	368.89
Hf	5.03	5.35	5.93	6.44	7.27	8.04	9.09	7.83	7.96	8.94	9.27	10.06	10.49	11.15	12.71	13.84	13.39	14.81	13.97	15.75	18.53	17.81	14.52
Ce	110.80	115.66	160.40	136.31	195.82	193.43	83.02	186.44	186.44	229.72	236.52	67.48	241.29	121.67	91.73	157.71	83.53	202.55	92.44	64.55	64.55	81.63	79.16
Pr	14.46	13.23	15.01	14.48	13.48	24.71	21.03	13.54	13.54	27.81	12.87	9.32	22.85	14.26	12.08	18.07	10.49	24.79	11.70	8.11	7.29	9.61	14.53
Nd	7.20	7.51	7.66	8.15	8.65	10.18	11.51	13.01	14.69	15.93	21.62	24.45	26.52	29.94	31.21	18.01	32.48	26.52	36.72	42.36	38.28	48.86	38.28
Sm	5.22	5.68	6.52	7.24	8.43	9.54	11.05	7.81	8.87	10.03	11.32	12.45	13.06	14.01	15.37	16.44	17.22	19.27	17.61	20.62	24.62	23.58	18.85
Eu	0.72	0.74	0.74	0.80	0.79	0.79	0.82	0.85	0.87	0.87	0.86	0.89	0.90	0.97	0.93	0.82	0.95	0.98	0.95	0.80	0.81	0.95	0.87
Gd	7.60	8.15	10.66	11.90	12.81	5.62	6.20	6.87	4.44	4.51	4.72	4.95	5.62	8.36	8.32	9.07	9.90	10.73	10.24	9.48	9.24	10.75	10.25
Tb	1.26	1.36	1.82	2.04	2.21	0.90	1.01	1.13	0.69	0.70	0.74	0.78	0.90	1.40	1.39	1.53	1.68	1.83	1.74	1.60	1.56	1.83	1.74
Dy	7.89	8.57	11.66	13.20	14.32	5.44	6.16	6.98	3.99	4.07	4.33	4.61	5.44	8.82	8.77	9.70	10.73	11.75	11.15	10.20	9.91	11.77	11.16
Ho	1.47	1.60	2.22	2.52	2.75	0.98	1.12	1.28	0.69	0.71	0.76	0.81	0.98	1.65	1.64	1.83	2.03	2.23	2.11	1.93	1.87	2.24	2.12
Er	4.43	4.86	6.82	7.79	8.50	2.87	3.33	3.85	1.95	2.01	2.17	2.35	2.87	5.02	4.99	5.57	6.23	6.87	6.49	5.89	5.71	6.89	6.50
Yb	3.43	3.84	5.69	6.61	7.28	1.96	2.39	2.88	1.09	1.14	1.30	1.46	1.96	3.99	3.96	4.51	5.13	5.74	5.38	4.81	4.64	5.76	5.39
Lu	0.50	0.56	0.84	0.98	1.08	0.28	0.35	0.42	0.15	0.16	0.18	0.21	0.28	0.59	0.58	0.67	0.76	0.85	0.80	0.71	0.69	0.85	0.80
Y	394.76	394.76	394.45	395.13	395.50	392.43	393.40	394.09	391.24	391.24	392.76	392.43	392.43	397.34	396.21	393.40	393.10	396.94	394.76	396.94	397.75	396.94	392.76
Petrochemical parameters																							
Mg#	13.88	10.52	11.75	11.47	14.94	9.85	16.63	10.10	11.99	8.44	14.19	10.31	9.81	3.34	5.73	2.90	8.70	8.73	11.72	9.45	8.21	26.89	9.10
FeOt/MgO	5.58	7.66	6.76	6.95	5.13	8.24	4.51	8.01	6.61	9.76	5.44	7.83	8.28	26.09	14.80	30.12	9.44	9.41	6.78	8.62	10.06	2.45	8.99
Rb/Th	0.73		0.79	0.81	0.81	0.81	0.82	0.82	0.87	0.90	0.90	0.90	0.93	0.93	0.93		0.93	1.02	1.08		1.09	1.05	1.06
Ba/Nb	0.73	0.65	0.65	0.45	0.61	0.58	0.56	0.51	0.59	0.62	0.61	0.59	0.53	0.51	0.50		0.53	0.56	0.49	0.44	0.49	0.51	0.46
Sr/Zr	0.19		0.15	0.13	0.10	0.10	0.08	0.08	0.08	0.06	0.04	0.07	0.07	0.04	0.04		0.03	0.03	0.03		0.02	0.01	0.02
Sr/Th	0.32		0.32	0.26	0.24	0.28	0.23	0.20	0.23	0.18	0.13	0.24	0.25	0.16	0.16		0.14	0.17	0.16		0.09	0.09	0.13
Nb/Ta	11.00	10.96	11.03	11.03	11.03	11.08	11.02	11.06	10.84	11.14	10.65	11.13	11.57	10.93	11.31	11.23	11.36	10.87	11.38	11.54	10.93	11.31	11.58
Lu/Yb	0.15		0.15	0.15	0.15	0.14	0.15	0.15	0.14	0.14	0.14	0.14	0.14	0.15	0.15		0.15	0.15	0.15		0.15	0.15	0.15
Th/La	0.48		0.48	0.47	0.43	0.40	0.43	0.43	0.40	0.44	0.41	0.49	0.49	0.44	0.44		0.52	0.39	0.39		0.42	0.42	0.44
Th/Ce	0.64		0.43	0.51	0.36	0.36	0.86	0.39	0.37	0.30	0.29	1.05	0.29	0.56	0.77		0.87	0.34	0.72		1.05	0.82	0.82
Rb/Th	23.46	23.84	23.87	23.11	23.84		30.29	22.74	30.26	30.72	39.49	35.36	35.43	37.27	38.36	35.92		64.16	66.19	67.19	80.68	72.49	71.41
Sr/Th	8479.37	5244.41	3973.72	3276.15	3025.96		7700.70	6305.17	3808.00	2223.75	2801.51	2740.89	2725.16	2596.52	2581.62	2552.07		3469.70	3965.44	3305.92	4784.01	4789.52	5021.02
Ta/Hf	0.01	0.03	0.03	0.03	0.04		0.06	0.10	0.08	0.10	0.15	0.15	0.14	0.16	0.17	0.18		0.15	0.15	0.14	0.16	0.17	0.18
Ta/U	1.46	1.31	1.35	1.24	1.17		1.24	1.24	1.21	1.49	1.21	1.88	1.88	2.11	1.35	2.08		1.56	1.56	1.42	1.71	1.75	1.58
Ta/Yb	0.04	0.06	0.03	0.04	0.04		0.05	0.08	0.04	0.06	0.08	0.08	0.07	0.08	0.07	0.07		0.09	0.11	0.07	0.09	0.08	0.10
Th/Ce	0.00	0.00	0.00	0.00	0.00		0.00	0.01	0.00	0.00	0.01	0.01	0.01	0.01	0.01	0.01		0.01	0.01	0.01	0.01	0.01	0.01
Th/La	0.01	0.01	0.01	0.01	0.01		0.01	0.01	0.01	0.01	0.02	0.02	0.02	0.02	0.02	0.02		0.02	0.02	0.02	0.01	0.02	0.02
Th/Nb	0.11	0.11	0.11	0.11	0.11		0.09	0.16	0.15	0.13	0.12	0.12	0.13	0.12	0.13	0.15		0.09	0.09	0.10	0.08	0.08	0.11
Th/Ta	1.41	1.46	1.50	1.53	1.55		1.19	1.56	1.58	1.40	1.32	1.27	1.41	1.29	1.47	1.46		0.92	0.97	1.11	0.80	0.89	1.11
Th/Yb	0.06	0.09	0.04	0.07	0.06		0.06	0.13	0.06	0.08	0.11	0.10	0.10	0.10	0.10	0.10		0.08	0.10	0.08	0.07	0.07	0.12
U/Th	0.49	0.53	0.49	0.53	0.55		0.68	0.52	0.53	0.48	0.62	0.42	0.38	0.37	0.50	0.33		0.70	0.66	0.64	0.73	0.65	0.57
Zr/Hf	4.12	9.45	11.59	11.73	11.89		19.27	24.17	30.88	39.03	25.68	25.05	26.81	26.68	31.10	32.92		29.05	29.10	35.59	34.53	38.22	28.79
Normative components																							
Quartz (Q)	29.50	27.36	27.13	27.69	31.39	29.45	28.58	30.34	31.48	31.71	29.48	28.70	27.85	29.70	30.43	28.83	28.79	28.10	29.15	29.66	30.53	30.61	31.84
Corundum(C)	1.06	0.17	0.00	0.08	1.11	0.00	0.00	0.26	0.55	0.00	0.41	0.00	0.00	0.00	0.00	0.00	0.00	0.00	0.00	0.00	0.00	0.00	0.00
Orthoclase(Or)	24.15	26.46	24.99	27.01	22.52	25.93	26.36	25.62	24.62	24.62	26.94	27.16	30.00	27.24	28.59	32.97	32.67	35.01	33.94	34.02	30.91	30.66	29.42
Albite(Ab)	33.59	35.12	36.64	34.95	34.52	35.45	35.88	34.44	34.05	33.97	35.29	37.15	36.51	37.32	35.77	30.41	30.94	31.26	29.80	28.44	31.68	32.11	31.64
Anorthite(An)	6.52	6.23	6.25	5.87	5.68	2.12	4.96	4.90	4.51	4.30	4.14	3.75	2.09	2.74	0.00	0.00	0.00	0.00	0.00	0.00	0.00	0.00	0.00

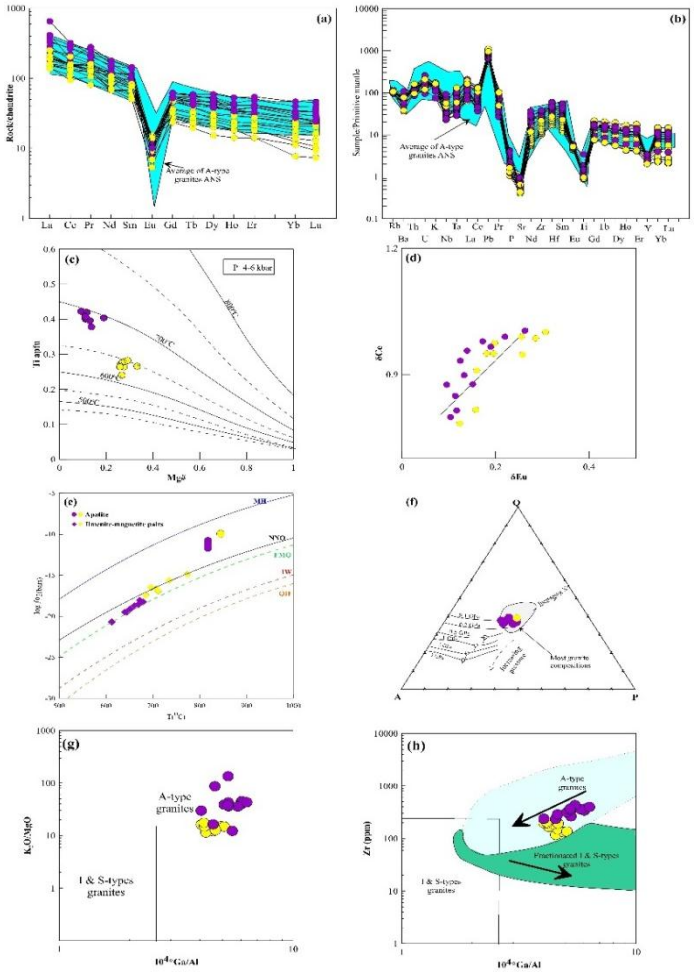

Fig. 8. Trace elements abundances. (a) Chondrite-normalized REE patterns for the studied granitic rocks; and (b) Primitive mantle-normalized multi-element patterns of trace elements in the studied granitic rocks. Primitive mantle concentrations from **(Sun & McDonough, 1989)** . Fields of the A-type granite suites from the ANS are adopted from **(Sami *et al.*, 2017)**; (c) Ti-in-biotite geothermometer **(Henry *et al.*, 2005)**. The dashed curves represent the intermediate 50 ℃ interval isotherms. Symbols in the diagram show the Ti(apfu.) vs. Mg# =[Mg/(Mg+Fe)] of biotites from AKAG; (d) Plots of δCe vs. δEu, for the apatite from AKAG; (e) L*gf*(O2) vs T (◦C) diagram of the AKAG. Abbreviation: Ap = apatite; Ilm = ilmenite; Mag = magnetite; Zir = zircon; MH = Magnetite-hematite bufffer; NNO = Nickel-nickel oxide bufffer; FMQ = Fayalite-magnetite-quartz bufffer; IW = Iron-wustite bufffer; QIF = Quartz-iron-fayalite buffer; (f) The normative Ab–Or–Qz diagram after **Tuttle and Bowen (1958)**; (g) MgO/K_2O and (h) Zr vs. $10^4 \times Ga/Al$ discrimination diagrams after (Whalen et al., 1987) the nested trends arrows and fields after (Wu et al., 2017) for the studied AKAG.

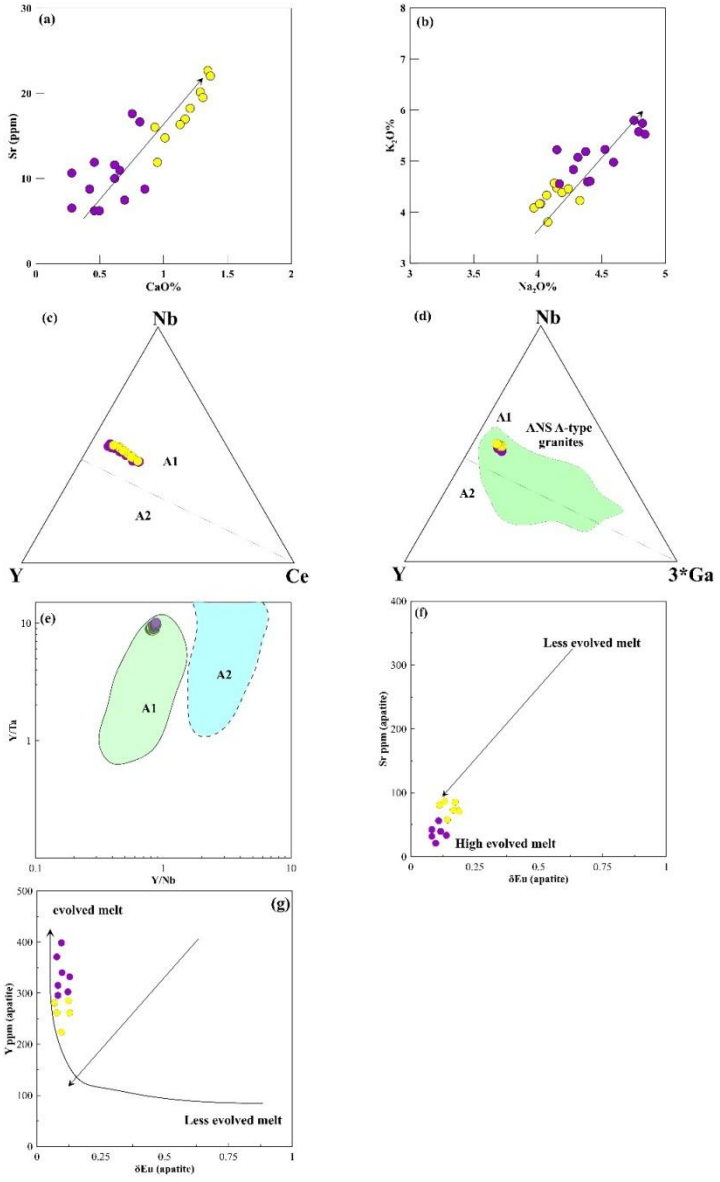

Fig. 9. Variation diagrams of AKAG. (a) Variation diagram of whole rock contents of Sr vs. Cao Wt.%; (b) Whole rock variation diagram of K2O vs. Na2O of the AKAG; (c) Nb-Y-3Ga; and (d) Nb-Y-Ce; (e) Y/Nb vs. Y/Ta; discrimination diagrams (Eby, 1990) for AKAG; (f) and (g) Plots of Sr, and Y vs. δEu values of the apatite from AKAG. Chondrite normalized values are from (Sun and McDonough, 1989).

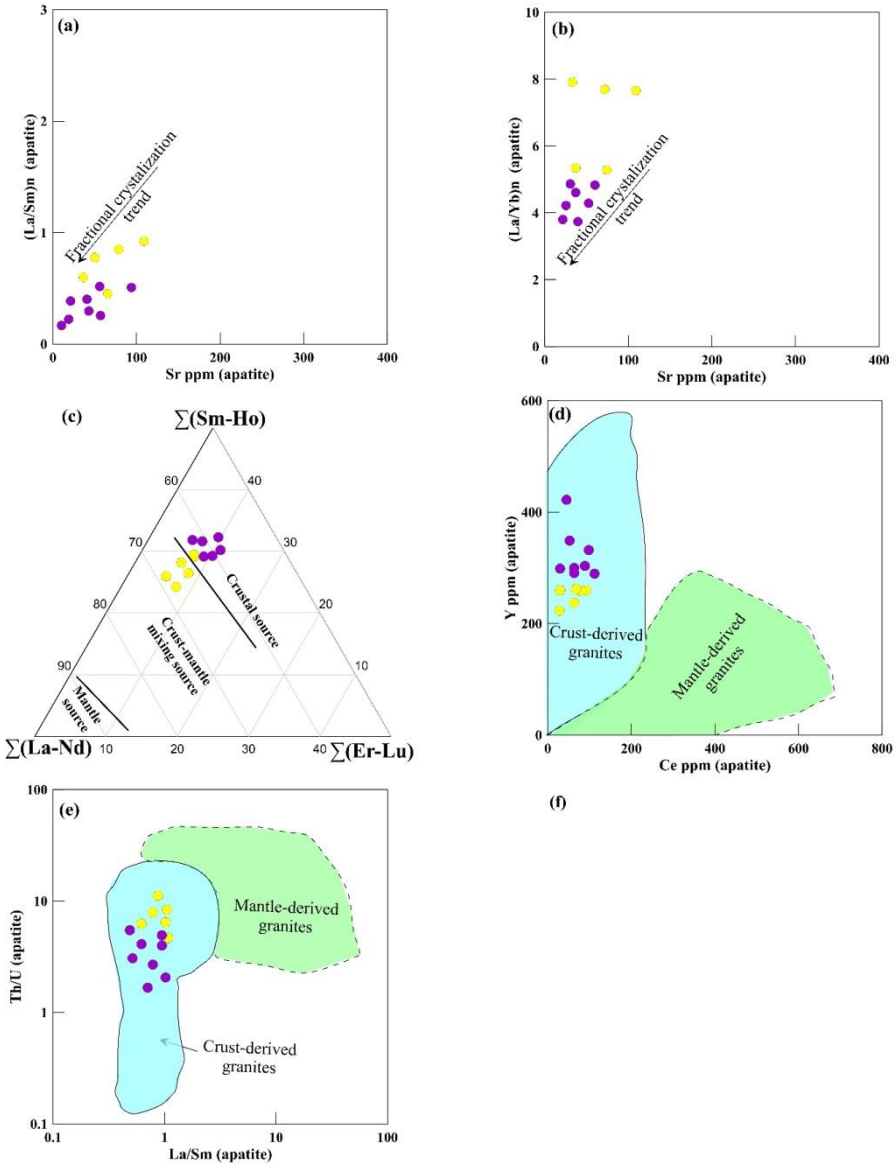

Fig. 10. Plots of (a) (La/Yb)n, and (b) (La/Sm)n vs Sr contents of the apatite within AKAG; (c) Σ(La–Nd) - Σ(Sm–Ho) - Σ(Er–Lu) ternary diagram (**Zhu and Chen, 2004)** for magmatic apatite apatite from AKAG; Plots of (d) Y vs Ce contents, and (e) Th/U vs La/Sm ratios for the analysed apatite from AKAG.**(Laurent *et al.*, 2017).**

All apatite samples display low Ce/Pb (0.06-0.395) and Th/U (1.87-12.37) which strongly reflects fluid and or crustal material involvement during crystallization **(Kogiso, *et al.*, 1997)**. Moreover, the apatite composition of the AKAG broadly span from fields indicative of crust–mantle mixing to those representing predominantly crustal source, implying that the genesis of the AKAG involved partial melting of crustal sources, followed by a prolonged phase of fractional crystallization that led to its evolved composition. This conclusion is confirmed from the whole rock chemical analysis, where the analysed samples of AKAG demonstrating surplus concentrations of Na, K, Rb and Pb, whereas possess low concentrations Eu, Sr and Ti **(Bonin, 2007; Elsagheer, *et al.*, 2023)**. Moreover, the AKAG apatite exhibits Ce/Y, Th/U, and La/Sm ratios that align with the compositional characteristics of crust-derived granitoids (Fig. 10 d, e).

CONCLUSION

The petrological and mineralogical characteristics of the alkaline granites of Abu Kharif complex exemplify the characteristic features of typical anorogenic alkaline magmatism that have intruded into the frame of proto-Arabian-Nubian Shield spanning. The alkaline granites of Abu Kharief Constitute syenogranite and alkali feldspar granite exhibiting prominent alkaline nature. Mineral chemistry of biotite, apatite and iron oxides reveal that these rocks were emplaced at relatively low pressure (1.03-1.08 kbar for syenogranite and 1.08-1.12 kbar for alkali feldspar granite). Thermometric estimates based on coexisting magnetite–ilmenite assemblages suggest equilibrium temperatures ranging from 685–744 °C for SG and 612-680 °C for AKG indicating either late-stage cooling or subsolidus re-equilibration. Apatite chemical data strongly reflects fluid and crustal material involvement during crystallization. Their apatite saturation temperatures range from 768-902°C, which consistent with the crystallization temperature that deduce from the whole rock geochemical data (724°C to 902°C, with an average of ~847 °C). where these values are in good agreement with previously reported temperatures for post-collisional granitic intrusions within the ANS.

Acknowledgement

The author extends his sincere appreciation to Dr. David Orejendka of the geology department of Complutense university, Madrid, Spain for his invaluable assistance with the electron probe microanalysis (EPMA) measurements. Additionally, the author conducted this study during a six-month scientific mission in Complutense University, Spain; funded by the Egyptian Missions Sector. We are also grateful to the Egyptian Ministry of Higher Education and Scientific Research for their continued support.

REFERENCES

Abdel-Rahman, A. (2006): Petrogenesis of anorogenic peralkaline granitic complexes from eastern Egypt. Mineralogical Magazine, 70(1), 27-50.

Abdel-Rahman, A.M. (1994): Nature of biotites from alkaline, calc-alkaline, and peraluminous magmas. J. Petrol., 35(2): 525-541.

Abdel-Rahman, A.F.M. and R.F. Martin (1987): Late Pan-African magmatism and crustal development in northeastern Egypt. Geological J., 22(4): 281-301.

Abdel Aal, A. (1996): Proterozoic A-type granite: A study from the northeastern Nubian Shield, Egypt. Egyptian J. Geol., 40: 631-659.

Abdel Wanees, N.G. ; M.M. El-Sayed ; K.I. Khalil and H.A. Khamis (2021): Petrogenesis of contrasting magmatic suites in the Abu Kharif area, Northern Eastern Desert, Egypt: implications for Pan-African crustal evolution and tungsten mineralization. Geological Magazine, 159(3): 441-467.

Abdelfadil, K.M. ; M.E. Gharib ; P. Uher and M. Putiš (2022): Petrogenesis of post-orogenic Pan-African rare-element granitic pegmatites in the western Arabian-Nubian Shield, Aswan area, southern Egypt. J. Asian Earth Sci., 224: 105003.

Ali, B. ; S. Wilde and M. Gabr, (2009): Granitoid evolution in Sinai, Egypt, based on precise SHRIMP U–Pb zircon geochronology. Gondwana Res., 15(1): 38-48.

Ali, K.A. ; A.K.M. Moghazi ; A.E. Maurice ; S.A. Omar ; Q. Wang ; S.A. Wilde and R.J. Stern (2012): Composition, age, and origin of the~ 620 Ma Humr Akarim and Humrat Mukbid A-type granites: No evidence for pre-Neoproterozoic basement in the Eastern Desert, Egypt. Int. J. Earth Sci., 101(7), 1705-1722.

Andersen, D. (1985). New (and final!) models for the Ti-magnetite/ilmenite geothermometer and oxygen barometer. Paper presented at the Abstracts of American Geophysical Union 1985 Spring Meeting.

Asran, A.M. ; A. Emam and A. El-Fakharani (2017): Geology, structure, geochemistry and ASTER-based mapping of Neoproterozoic Gebel El-Delihimmi granites, Central Eastern Desert of Egypt. Lithos, 282: 358-372.

Azadbakht, Z. ; D.R. Lentz and C.R.M. McFarlane (2018). Apatite Chemical Compositions from Acadian-Related Granitoids of New

Brunswick, Canada: Implications for Petrogenesis and Metallogenesis. Minerals, 8(12). doi:10.3390/min8120598

Azer, M. ; K. Abdelfadil and A. Ramadan (2019): The Nuweibi rare-metal albite granite: A magmatic cupola above a highly fractionated post-collisional A-type granite pluton. J. Geol., 10, x.

Azer, M.K. ; B.A. Abuamarah ; M.M. Srour ; S.A. Wilde and R.M. Gomaa (2023): Mineralogy, Geochemistry, and Petrogenesis of Postcollisional Granites from the Arabian-Nubian Shield: Case Study from the Gabal Nugrus Area in the South Eastern Desert of Egypt. J. Geol., 131(3): 221-263.

Ballard, J.R. ; J.M. Palin and I.H. Campbell (2002): Relative oxidation states of magmas inferred from Ce(IV)/Ce(III) in zircon: application to porphyry copper deposits of northern Chile. Contributions to Mineral. and Petrol., 144(3): 347-364.

Barker, F. and J.G. Arth (1976): Generation of trondhjemitic-tonalitic liquids and Archean bimodal trondhjemite-basalt suites. Geol., 4(10): 596-600.

Be'eri-Shlevin, Y. ; Y.Katzir and M. Whitehouse (2009): Post-collisional tectonomagmatic evolution in the northern Arabian–Nubian Shield: time constraints from ion-probe U–Pb dating of zircon. J. Geological Society, 166(1): 71-85.

Belousova, E.A. ; W.L.Griffin ; S.Y. O'Reilly and N.I. Fisher (2002): Apatite as an indicator mineral for mineral exploration: trace-element compositions and their relationship to host rock type. J. Geochemical Exploration, 76(1): 45-69.

Bonin, B. (2007): A-type granites and related rocks: Evolution of a concept, problems and prospects. Lithos, 97(1), 1-29.

Buddington, A. and D. Lindsley (1964): Iron-titanium oxide minerals and synthetic equivalents. J. Petrol., 5(2): 310-357.

Chappell, B. (1999): Aluminium saturation in I-and S-type granites and the characterization of fractionated haplogranites. Lithos, 46(3): 535-551.

Chen, M. ; L. Bagas ; X. Liao ; Z. Zhang and Q. Li (2019): Hydrothermal apatite SIMS ThPb dating: Constraints on the timing of low-temperature hydrothermal Au deposits in Nibao, SW China. Lithos, 324-325, 418-428.

Chu, M.F. ; K.L. Wang ; W.L. Griffin ; S.L. Chung ; S.Y. O'Reilly ; N.J. Pearson and Y. Iizuka (2009): Apatite Composition: Tracing Petrogenetic Processes in Transhimalayan Granitoids. J. Petrol., 50(10): 1829-1855.

Daneshvar, N. ; H. Azizi and M. Tsuboi (2022): Estimating magma crystallization temperatures using high field strength elements in igneous rocks. Minerals, 12(10). doi:10.3390/min12101260

Deer, W.A. ; R.A. Howie and J. Zussman (1992): An Introduction to the Rock-Forming Minerals. 2nd Edition, Prentice Hall, Harlow. New York.

Dessouky, O. K. ; H. Li ; H.H. Ali ; A.M. Dardier ; K.A. Ali ; F. Pirajno and M.M. Hassan (2024): Ediacaran anorogenic alkaline magmatism and wolframite mineralization linked to mantle plume activity in the north Arabian-Nubian Shield (Egypt). Geochem., 84(3). doi:10.1016/j.chemer.2024.126119

Dorais, M.J. and C.J. Spencer (2014): Revisiting the importance of residual source material (restite) in granite petrogenesis: The Cardigan Pluton, New Hampshire. Lithos, 202-203, 237-249. doi:https://doi.org/10.1016/j.lithos.2014.05.007

Eby, G.N. (1990): The A-type granitoids: A review of their occurrence and chemical characteristics and speculations on their petrogenesis. Lithos, 26(1): 115-134.

Eby, G.N. (1992): Chemical subdivision of the A-type granitoids: petrogenetic and tectonic implications. Geology, 20(7), 641-644.

El-Awady, A. ; M. Sami ; R. Abart ; D. Fathy ; E.S. Farahat ; M.S. Ahmed and A. Ragab (2024). Petrogenesis and Tectonic Evolution of I- and A-Type Granites of Mount Abu Kibash and Tulayah, Egypt: Evidence for Transition from Subduction to Post-Collision Magmatism. Minerals, 14(8). doi:10.3390/min14080806

El-Bialy, M. ; H. Eliwa ; N. Mahdy ; M. Murata ; K. El-Gameel ; H. Sehsah and A. Andresen (2020): U-Pb zircon geochronology and geochemical constraints on the Ediacaran continental arc and post-collision granites of Wadi Hawashiya, North Eastern Desert, Egypt: insights into the~ 600 Ma crust-forming event in the northernmost part of Arabian-Nubian Shield. Precambrian Res., 105777.

El-Bialy, M.Z. and M.M. Omar (2015): Spatial association of Neoproterozoic continental arc I-type and post-collision A-type granitoids in the Arabian–Nubian Shield: the Wadi Al-Baroud older and younger granites, north eastern desert, Egypt. J. African Earth Sci., 103: 1-29.

El-Gaby, S. (2007): Integrated classification and evolution of the Neoproterozoic Pan-African Belt in Egypt. The Fifth Int. Conference on the Geol. of Africa, 1: 143-154.

El-Shazly, S.M. and M.M. El-Sayed (2000): Petrogenesis of the Pan-African El-Bula Igneous Suite, central Eastern Desert, Egypt. J. African Earth Sci., 31(2): 317-336.

El Bahariya, G. (2019). Geochemistry and Tectonic Setting of Neoproterozoic Rocks from the Arabian-Nubian Shield: Emphasis on the Eastern Desert of Egypt. In F. L. Mazadiego, E. De Miguel Garcia, F. Barrio-Parra, & M. Izquierdo-Diaz (Eds.), Applied Geochemistry with Case Studies on Geological Formations, Exploration Techniques and Environmental Issues. Rijeka: IntechOpen.

Eliwa, H.A. ; C. Breitkreuz ; M. Murata ; I.M. Khalaf ; B. Bühler ; T. Itaya and T. Shibata (2014): SIMS zircon U–Pb and mica K–Ar geochronology, and Sr–Nd isotope geochemistry of Neoproterozoic granitoids and their bearing on the evolution of the north Eastern Desert, Egypt. Gondwana Res., 25(4): 1570-1598.

Elsagheer, M.A. ; M.K. Azer ; A.E. Maurice ; A.E.S. Khalil and M.M.N. Taha (2023): Geochemistry and origin of felsites and associated A-type granites at Wadi Atalla area, Central Eastern Desert, Egypt: Implication for genesis of Neoproterozoic post-collisional highly silicic melts. Geochemistry, 125987.

Farahat, E. ; H. Mohamed ; A. Ahmed and M. El Mahallawi (2007): Origin of I- and A-type granitoids from the Eastern Desert of Egypt: implications for crustal growth in the northern Arabian–Nubian Shield. J. African Earth Sci., 49(1-2): 43-58.

Farahat, E.S. and M. K.Azer (2011): Post-collisional magmatism in the northern Arabian-Nubian Shield: The geotectonic evolution of the alkaline suite at Gebel Tarbush area, south Sinai, Egypt. Geochemistry, 71(3): 247-266.

استقصاء الظروف الفيزيائية والكيميائية للصهارة في جرانيت أبو خريف القلوي، شمال الصحراء الشرقية، مصر، باستخدام كيميائية الأباتيت والماجنتيت والإلمانيت

مصطفى محمد مجاهد أحمد

قسم الجيولوجيا – كلية العلوم – جامعة بنها

يتكون مركب جرانيت أبو خريف القلوي (AKAG) في الصحراء الشرقية الشمالية من السيينوجرانيت وجرانيت الفلسبار القلوي. وعلى الرغم من أن النشأة الصخرية لهذه الصخور موثقة جيدًا في الأدبيات الجيولوجية، إلا أن الظروف الفيزيائية والكيميائية لها لم تتم دراستها خصوصا استنادًا إلى التركيب الكيميائي لمكوناتها المعدنية. تُصنّف البيانات الجيوكيميائية لصخور AKAG لى أنها من النوع A عالي التمايز وذو ميل قلوي وتنتمي إلى النمط الفرعي

A1.تم استخدام كيمياء المعادن لكل من الفلسبارات، والبيوتيت، والأباتيت، وأكاسيد الحديد لتحديد الظروف الفيزيائية والكيميائية وتطور الجرانيت القلوي.

أظهرت البيانات الجيوكيميائية للصخور الكاملة أن هذه الصخور تمتلك قيم (La/Sm)□ تتراوح بين 1.71 و4.52، ونقصًا طفيفًا في العناصر الأرضية النادرة الثقيلة HREEs ($(Gd/Yb)_n$ = 1.34–3.11)، وشذوذ سلبي واضح في عنصر اليوروبيوم (Eu/Eu* = 0.09–0.37)، وهي سمات مميزة للجرانيتات عالية التمايز من النوع A . تشير نتائج مقياس حرارة البيوتيت إلى أن نطاق تبلور هذه الصخور يقع بين 610 و700 درجة مئوية عند معاملات تأكسد (logfO2) تتراوح بين −11.91 و−12.63، مما يدل على تبلور من صهارة مؤكسدة نسبيًا، وهو ما يتماشى مع التمعدن في ظروف ضغط منخفض.

أظهرت البيانات الكيميائية للماجنتيت، والإلمانيت، والأباتيت أن ظروف الأكسدة في صهارة AKAGكانت أعلى قليلًا من خط عازلΔNNO ، وأن الماجنتيت والإلمانيت كانا مستقرين عند درجات حرارة بين 571 678 درجة مئوية، مما يشير إلى أن مستويات الأكسجين قد انخفضت مع تطور الصهارة. تُظهر أنماط العناصر الأرضية النادرة (REE) في الأباتيت من AKAG زيادة معتدلة إلى قوية في العناصر الخفيفة مثلLa ، Ce، وPr، إلى جانب انخفاض طفيف إلى معتدل في(Eu/Eu* < 1) Eu ، مما يشير على الأرجح إلى فصل البلاجيوكليز أثناء تطور الصهارة.